WILEY-VCH

Supporting Information

Micro-Corrugated Hydrogel Electrodes for High-Performance Biofuel Cells via Capillary Force and Ligand Exchange-Induced Metal Nanoparticle Assembly

Eunju Choi[1§], Jun Hyung Kim[1§], Su Hwan Kim[1], Hye Min Yu[1], Gee Chan Jin[1], Jeongmin Mo[2], Junha Pak[2], Seung-Kyum Choi[3], Jongkuk Ko[4], Jinhan Cho[2,5*], and Cheong Hoon Kwon[1*]*

[1]Department of Energy Resources and Chemical Engineering, Kangwon National University, 346 Jungang-ro, Samcheok, 25913, Republic of Korea

[2]Department of Chemical & Biological Engineering, Korea University, 145 Anam-ro, Seongbuk-gu, Seoul 02841, Republic of Korea

[3]GeorgeW. Woodruff School of Mechanical Engineering, Georgia Institute of Technology, Atlanta, GA, USA

[4]School of Chemical, Biological, and Battery Engineering, Gachon University, 1342 Seongnam-daero, Seongnam si, Gyeonggi-do 13120, Republic of Korea

[5]KU-KIST Graduate School of Converging Science and Technology, Korea University, 145 Anam-ro, Seongbuk-gu, Seoul 02841, Republic of Korea

*Address correspondence to chkwon2@kangwon.ac.kr, jinhan71@korea.ac.kr and kojk@gachon.ac.kr

[§]These authors equally contributed to this work.

Experimental Section

***Materials*:** Acrylic acid, Acrylamide, Ethylene glycol dimethylacrylate (EGDMA), Dimethyl Sulfoxide (DMSO), 2,2-Dimethoxy-2-phenyl-acetophenone, Tetraoctylammonium bromide (TOABr), gold(III) choloride trihydrate ($HAuCl_4 \cdot 3H_2O$), sodium borohydride ($NaBH_4$), tris-(2-aminoethyl)amine (TREN) (Mw ~146 g mol^{-1}) and polyethylenimine, branced (PEI, Mw ~800 and ~25,000 g mol^{-1}), chloroplatinic acid hexahydrate (H_2PtCl_6) were purchased from Sigma Aldrich. Glucose oxidase (GOx) from Aspergillus niger (180 U mg^{-1}) was purchased from Amano Enzyme Inc. (Japan).

***Synthesis of PEI-hydrogel*:** First, acrylic acid and acrylamide were dissolved in deionized water at a molar ratio of 4:1 (12 and 3 mmol L^{-1}, respectively). Then, 200 μl of EGDMA and 30 mg of 2,2-Dimethoxy-2-phenyl-acetophenone dissolved in DMSO, which served as cross-linker and initiator, respectively, were added to the aqueous solution of acrylic acid and acrylamide.[S1] The prepared solution was confined within a polyethylene terephthalate (PET) frame with a specific thickness (250 μm) sandwiched between slide glasses. The ultraviolet light was irradiated for 30 min to polymerize the confined solutions. Then, we got PAA-co-PAAm hydrogel film. And the PAA-co-PAAm hydrogel was immersed in aqueous PEI solutions (20 mg mL^{-1}) for more than 24 h. Because of infiltration of the PEI into the hydrogel matrix, the hydrogel films were swollen depending on the concentrations of PEI solutions.

***Synthesis of TOA-Au NPs*:** Tetra(octylammonium) (TOA)-stabilized Au nanoparticles (NPs) with a diameter of 8 nm were synthesized by a two-phase method in toluene.[S2] Initially, $HAuCl_4 \cdot 3H_2O$ in deionized water (30 mmol L^{-1}, 30 mL) and TOA stabilizers in toluene (20 mmol L^{-1}, 80 mL) were vigorously stirred together. Subsequently, $NaBH_4$ solution in water (400 mmol L^{-1}, 25 mL) was added to the two-phase mixture. After stirring for approximately 2.5 h, the aqueous phase was separated, and the remaining toluene solution was repeatedly washed with dilute aqueous H_2SO_4 (100 mmol L^{-1}), NaOH (100 mmol L^{-1}), and deionized

water. Finally, following several washing steps and the removal of the aqueous solution, a suspension of TOA-Au NPs dispersed in toluene (~10 mg mL^{-1}) was obtained.

***Synthesis of citrate Au NPs*:** Citrate ion-stabilized Au NPs (citrate Au NPs) with average diameters of 23 nm were synthesized.[S3-S4] Briefly, a 100 mL sample of aqueous $HAuCl_4$ (0.1 mmol L^{-1}) was put into a 250 mL flask at room temperature. The solution was heated to its boiling point (~90 °C) under magnetic stirring (750 rpm), and after it started to boil, 1.2 mL of sodium citrate solution (50 mg mL^{-1}) was added. The reaction was allowed to proceed until the solution became wine red in color (approximately 5 min). After the color change ceased, the solution was gradually cooled to room temperature.

***Preparation of TOA-Au NPs hydrogel (i.e., TAH)*:** PEI-hydrogel was dipped into a toluene solution containing TOA-Au NPs. With increasing deposition time of TOA-Au NPs, the adsorbed Au NPs were converted into a mesoporous Au nanoflake by capillary force and ligand exchange-induced metal nanoparticle assembly between PEI and TOA-Au NPs. Moreover, the dipping times were varied (12, 24, 48, and 72 h) to control deposition.

***Preparation of citrate Au NPs hydrogel*:** The PEI-hydrogel was placed in a vial containing an aqueous solution of citrate Au NPs and immersed overnight at room temperature while shaking at 120 rpm using a shaker. The hydrogel remained fully submerged in the solution throughout the process to ensure continuous contact with the dispersed nanoparticles. The mild agitation facilitated uniform exposure of the hydrogel surfaces to the citrate Au NPs, which were gradually adsorbed onto the hydrogel matrix during the immersion.

***Preparation of Au-sputtered hydrogel*:** The PEI-hydrogel was completely dried at room temperature before the sputtering process. After drying, Au was deposited onto the hydrogel using a sputtering system (DADA Korea, South Korea). The sputtering was conducted for 30 seconds per side and repeated four times. Through this process, Au was coated uniformly on the surface of the hydrogel.

***Preparation of 5-MTAH*:** TAH was assembled with (TREN/TOA-Au NP)$_n$ multilayers using a layer-by-layer (LbL) approach. For each bilayer, the hydrogel was first immersed in a 10 mmol L^{-1} aqueous solution of TREN for 30 min to introduce amine functionalities, followed by rinsing with deionized water. Subsequently, the hydrogel was immersed in TOA-Au NPs for 30 minutes to allow ligand exchange and deposition of Au NPs onto the hydrogel surface, and washing again. This process was repeated for the desired bilayer number (n), typically n = 5.

***Preparation of 5-GOx-5-MTAH*:** 5-MTAH was first prepared as described above. For enzyme immobilization, LbL assembly method was employed. 5-MTAH was alternately immersed in an aqueous solution of GOx (10 mg mL^{-1}) and immersed in TOA-Au NPs. Each immersion step was carried out for 30 minutes at room temperature, and after each step, the electrode was thoroughly rinsed with the corresponding solvent (PBS or toluene) to remove any unbound materials. This process was repeated for m = 5 to construct (GOx/TOA-Au NP)$_5$ multilayers on the 5-MTAH.

***Preparation of Pt-5-MTAH*:** To prepare the Pt-modified metallic TOA-Au NPs hydrogel (Pt-5-MTAH), 5-MTAH was immersed in a 10 mmol L^{-1} aqueous solution of chloroplatinic acid (H_2PtCl_6) for 6 h at room temperature. Then, 0.3 mL of a freshly prepared 5 wt% $NaBH_4$ solution was slowly added into the chloroplatinic acid solution containing the immersed 5-MTAH. Finally, that electrode was washed with deionized water.

Electrical conductivity measurement: The sheet resistance of the dried hydrogel electrodes was measured using a four-point probe sheet resistance/resistivity measurement system (CMT-100 series, AIT Co., Ltd., South Korea). Prior to measurement, the hydrogels were dried to a constant weight and gently flattened to ensure intimate contact with the probe head. During the measurement, a constant current was applied through the outer two probes, and the resulting voltage drop between the inner probes was recorded using the built-in measurement

program. The sheet resistance (R_s) was calculated according to the standard four-point probe method, and the electrical conductivity (σ) was obtained from:

$$\sigma = \frac{1}{R_s \cdot t}$$

where t is the thickness of Au nanoplate film on hydrogel. The use of the four-probe configuration effectively minimizes errors arising from contact and lead resistances, thereby improving the reliability of the conductivity values. All measurements were repeated on at least three independently prepared samples, and the averaged values were reported.

***Electrochemical measurement*:** Electrochemical measurements were performed using a standard three-electrode system comprising hydrogel based working electrode, an Ag/AgCl (saturated KCl) reference electrode, and a platinum wire counter electrode. The working electrode was prepared by attaching the hydrogel electrode to a copper plate using commercially available silver paste (ELCOAT P-100, CANS, South Korea). After drying, the connection was insulated with epoxy adhesive to prevent electrical leakage during measurements. Cyclic voltammetry (CV) experiments were conducted on 5-MTAH. The potential was swept from −0.6 V to +0.6 V at a scan rate of 5 mV s^{-1} using an Ivium-n-Stat electrochemical analyzer (Ivium Technologies, Netherlands). All measurements were performed in batch mode using 50 mL of phosphate-buffered saline (PBS, 20 mmol L^{-1} phosphate, 140 mM NaCl, pH 7.4) at 36.5 °C without stirring. To prevent electrical leakage during continuous operation and power density measurements, one end of each hydrogel electrode was secured to a glass substrate using epoxy resin. Maximum anodic and cathodic current densities were determined by CV at constant potentials of +0.6 V (anode) and −0.6 V (cathode), respectively. Normalized current densities were calculated by subtracting background current densities measured in PBS solution without glucose (0 mmol L^{-1} glucose) for the anode and nitrogen-saturated PBS solution for the cathode. Power density

measurements of the hydrogel EBFCs were performed by recording current outputs across fixed external resistances ranging from 1 kΩ to 10 MΩ to control the cell potential. Electrochemical impedance spectroscopy (EIS) was carried out over a frequency range of 0.2 Hz to 100 kHz with a perturbation amplitude of 10 mV.

***Analysis of electron transfer kinetics using the Laviron model*:** The heterogeneous electron transfer rate constant (k_s) and electron transfer coefficient (α) for the electrode reactions were determined using the Laviron model based on CV data. CVs were recorded at various scan rates (v), and the peak anodic (E_{pa}) and cathodic (E_{pc}) potentials were extracted for each scan rate.[S5] For a surface-confined redox system exhibiting quasi-reversible electron transfer, the Laviron equations are as follows:

$$\Delta E_{Pc} = -\frac{RT}{\alpha nF}\ln\left(\frac{a}{|\mathrm{m}|}\right) = -\frac{RT}{\alpha nF}\ln\left(v\frac{\alpha nF}{RTk_s}\right) = -\frac{RT}{\alpha nF}\ln(v) - \frac{RT}{\alpha nF}\ln\left(\frac{\alpha nF}{RTk_s}\right)$$

$$= a_c x + b_c$$

$$a_c = -\frac{2.303RT}{\alpha nF}, \qquad b_c = -\frac{2.303RT}{\alpha nF}\log\frac{\alpha nF}{RTk_s}, \mathrm{x} = \log(v)$$

$$\Delta E_{Pa} = -\frac{RT}{(1-\alpha)nF}\ln\left(\frac{(1-\alpha)}{\mathrm{m}}\right) = -\frac{RT}{(1-\alpha)nF}\ln\left(v\frac{(1-\alpha)nF}{RTk_s}\right)$$

$$= -\frac{RT}{(1-\alpha)nF}\ln(v) - \frac{RT}{(1-\alpha)nF}\ln\left(\frac{(1-\alpha)nF}{RTk_s}\right) = a_a x + b_a$$

$$a_a = -\frac{2.303RT}{(1-\alpha)nF}, \qquad b_c = -\frac{2.303RT}{(1-\alpha)nF}\log\frac{(1-\alpha)nF}{RTk_s}, \qquad \mathrm{x} = \log(v)$$

$$\Delta\mathrm{E} = E_{pc} - E^{\circ} \text{ or } \Delta\mathrm{E} = E_{pa} - E^{\circ}$$

$$\log k_s = \alpha\log(1-\alpha) + (1-\alpha)\log\alpha - \log\left(\frac{RT}{nFv}\right) - \frac{\alpha(1-\alpha)nF\Delta E}{2.303RT}$$

The variables in the equations [R (universal gas constant, R= 8.314 J mol^{-1} K^{-1}), T (absolute temperature), α(charge transfer coefficient), F(faraday constant, = 96485 C), E (peak anodic potential), E_{pc} (peak cathodic potential), E°(apparent formal redox potential), k_s

(heterogeneous electron transfer rate constant), n (number of electron transferred, n = 2), a_a (anodic curve slope), b_a(anodic curve intercept), a_c (cathodic curve slope), b_c (cathodic curve intercept), ν (scan rate), and x (logarithm of scan rate)] were utilized in the generalization of the Laviron model for redox substances. The k_s can be computed by analyzing the intersection of two linear fits corresponding to the anodic and cathodic curves. According to the equation, the maximum current occurs at the same potential as the peak potential (E_{pa} and E_{pc}), which also corresponds to the peak of the dimensionless phase. In CV, the peak anodic and cathodic currents correspond to E_{pa} and E_{pc}, respectively. Notably, the peak current exhibited negligible dependence on the scan rate, confirming that the redox species were firmly immobilized on the electrode surface rather than diffusing freely in solution.

Characterization: Fourier-transform infrared (FTIR) spectroscopy (Spectrum Two FTIR Spectrometer, PerkinElmer) equipped with a diamond attenuated total reflection (ATR) module was used for all measurements. All spectra were collected in the diamond ATR specular mode with a spectral resolution of 4 cm^{-1}, and the raw data were processed and plotted using OMNIC spectral analysis software (OMNIC, Nicolet). For time-resolved analysis, PEI-hydrogel samples were immersed in the TOA-Au NP toluene solution for 2, 5, 10, 30, 60, and 120 min, respectively. After immersion, each sample was dried for 20 min under identical ambient conditions to minimize variations in water content and ATR penetration depth. FTIR spectra were then collected immediately after the controlled drying process.

X-ray photoelectron spectroscopy (XPS) (ESCALAB 250Xi, Thermo Scientific) analysis was performed on multilayer samples deposited on Si wafers that were pre-cleaned by standard RCA treatment for 10 min. The baseline layer was prepared by sequentially coating PEI (20 mg mL^{-1}) and acrylic acid (AA, 12 mmol L^{-1}), corresponding to the hydrogel formulation. For multilayer assembly, PEI (20 mg mL^{-1}) and TOA-Au NP dispersions (10 mg

mL^{-1}) were alternately deposited on the substrate, with each layer adsorbed for 2 h to ensure sufficient interfacial interaction for XPS measurement.

***Analysis of enzyme affinity using Michaelis–Menten behavior*:** To evaluate the biological affinity of immobilized GOx, we used the apparent Michaelis–Menten constant (K_M^{app}) calculated it according to the Lineweaver–Burk equation, based on CV data. CVs were recorded at low glucose concentration (0-10 mmol L^{-1}) as follows:

$$\frac{1}{i} = \left(K_M^{app}\right)\left(\frac{1}{C}\right) + \frac{1}{i_{m\,ax}}$$

where i is the current, i_{max} is the maximum current measured under saturated substrate conditions, and C is the glucose concentration.

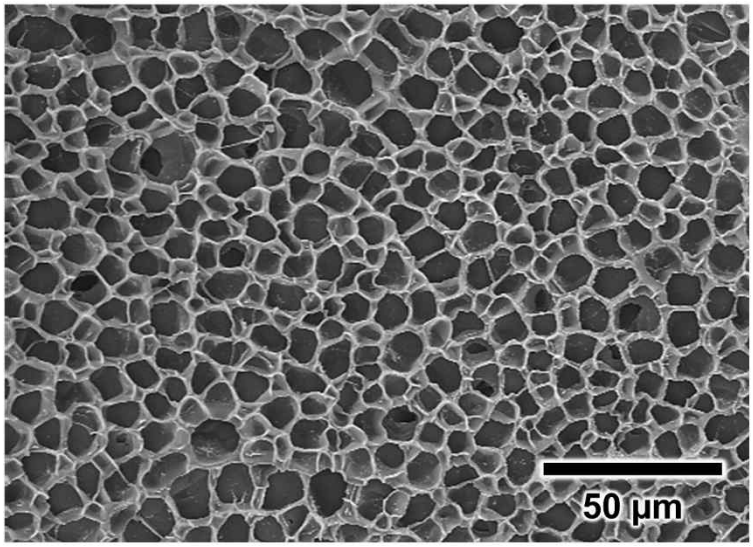

Figure S1. Porous structure of PAA-co-PAAm hydrogel. Field-emission scanning electron microscopy (FE-SEM) image of the freeze-dried PAA-co-PAAm hydrogel displays an interconnected porous structure with an average pore diameter of ~10 µm.

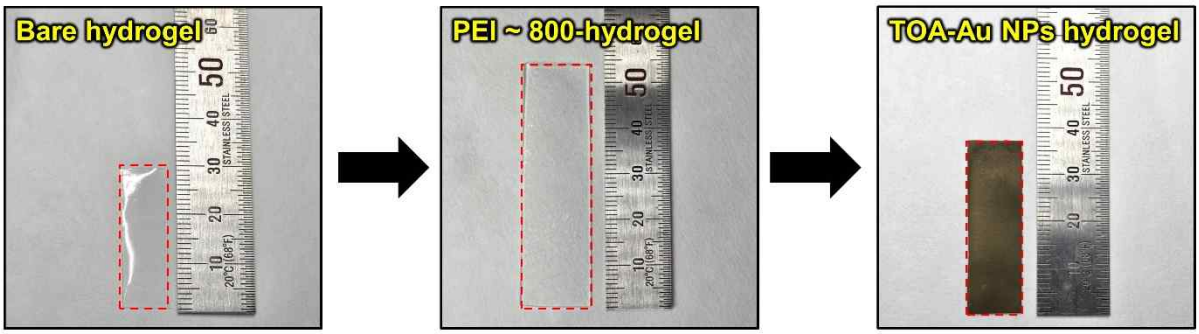

Hydrogels (Mw ~ 800)	Size (Length×Width×Height, cm)	Volume (cm^3)	Swelling ratio (%)
Bare hydrogel	1 × 3 × 0.25	0.75	0
PEI-hydrogel	1.8 × 5.4 × 0.54	5.25	600
TOA-Au NPs hydrogel	1.2 × 3.7 × 0.37	1.64	119

a

Figure S2. Photographic **images of bare hydrogel based on** PAA-co-PAAm, PEI ~ 800-hydrogel, and TOA-Au NPs hydrogel and each hydrogel's swelling/deswelling process.

b

a

b

Hydrogels (Mw ~ 25,000)	Size (Length×Width×Height, cm)	Volume (cm^3)	Swelling ratio (%)
Bare hydrogel	1 × 3 × 0.25	0.75	0
PEI-hydrogel	1.2 × 3.5 × 0.38	1.60	113
TOA-Au NPs hydrogel	1 × 3 × 0.27	0.81	8

Figure S3. Photographic images of bare hydrogel based on PAA-co-PAAm, PEI ~ 25,000-hydrogel, and TOA-Au NPs hydrogel and each hydrogel's swelling/deswelling process.

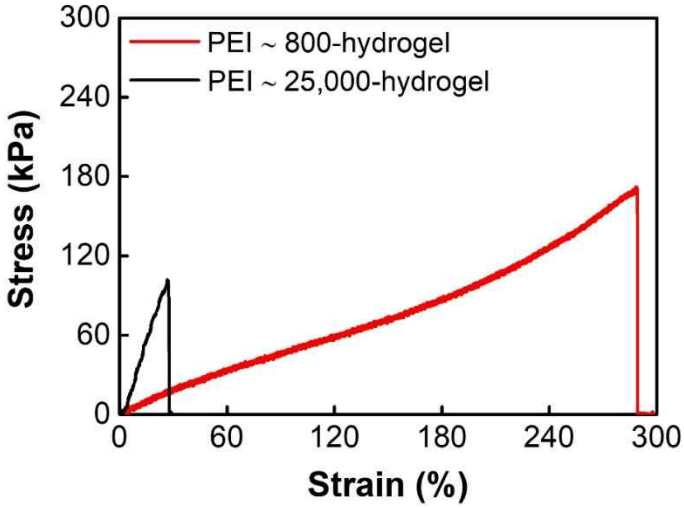

Figure S4. Stress–strain curves of hydrogels prepared with PEI ~ 800 and PEI ~ 25,000.

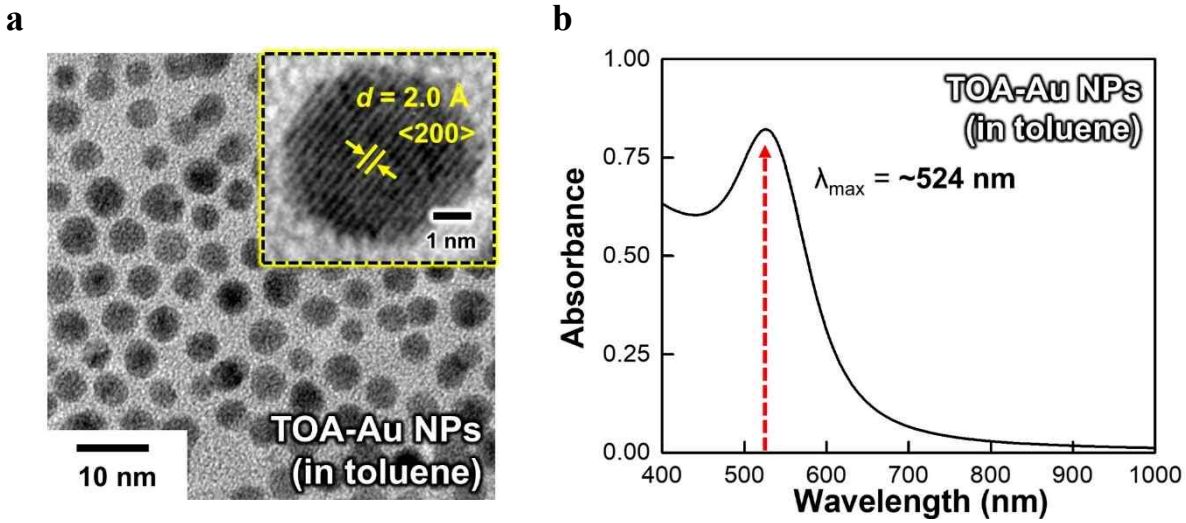

Figure S5. Characterization of TOA-Au NPs. a) High-resolution transmission electron microscopy (HR-TEM) images of TOA-Au NPs dispersed in toluene, revealing spherical particles with an average diameter of approximately 8 nm. b) UV-vis spectrum of TOA-Au NPs in toluene, showing a distinct localized surface plasmon resonance peak at ~524 nm, corresponding to well-dispersed and size-uniform nanostructures.

a

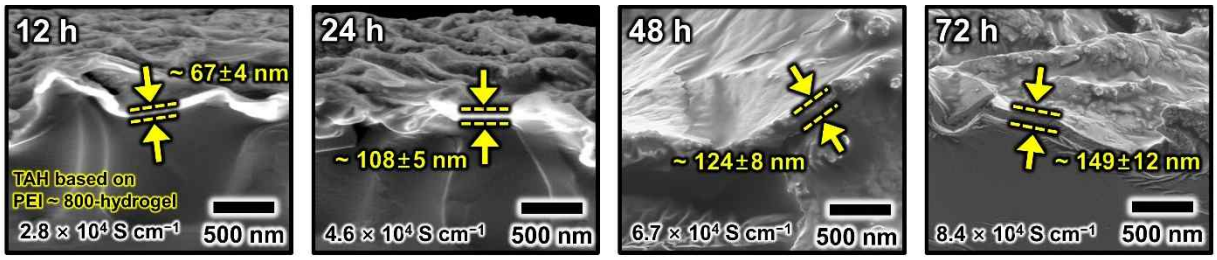

b

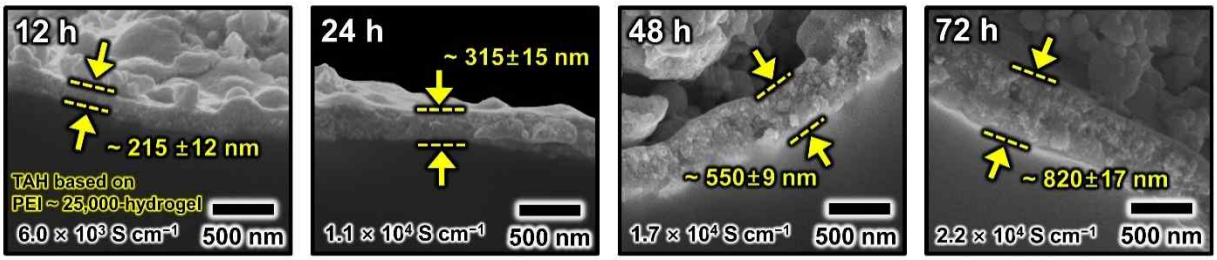

c

Loading Time (h)	Thickness (nm)	Sheet Resistance (Ω sq^{-1})	Electrical Conductivity (S cm^{-1})
TAH-based on PEI ~ 800			
12	~67 ± 4	5.7	2.8×10^4
24	~108 ± 5	2.0	4.6×10^4
48	~124 ± 8	1.2	6.7×10^4
72	~149 ± 12	0.8	8.4×10^4
TAH-based on PEI ~ 25,000			
12	~215 ± 12	7.8	6.0×10^3
24	~315 ± 15	3.0	1.1×10^4
48	~550 ± 9	1.1	1.7×10^4
72	~820 ± 17	0.6	2.2×10^4

Figure S6. Characterization of Au NP films with different PEI molecular weights. a) TAH-based on PEI ~ 800-hydrogel. b) TAH-based on PEI ~ 25,000-hydrogel. c) Comparison of film thickness, sheet resistance, and electrical conductivity as a function of loading time.

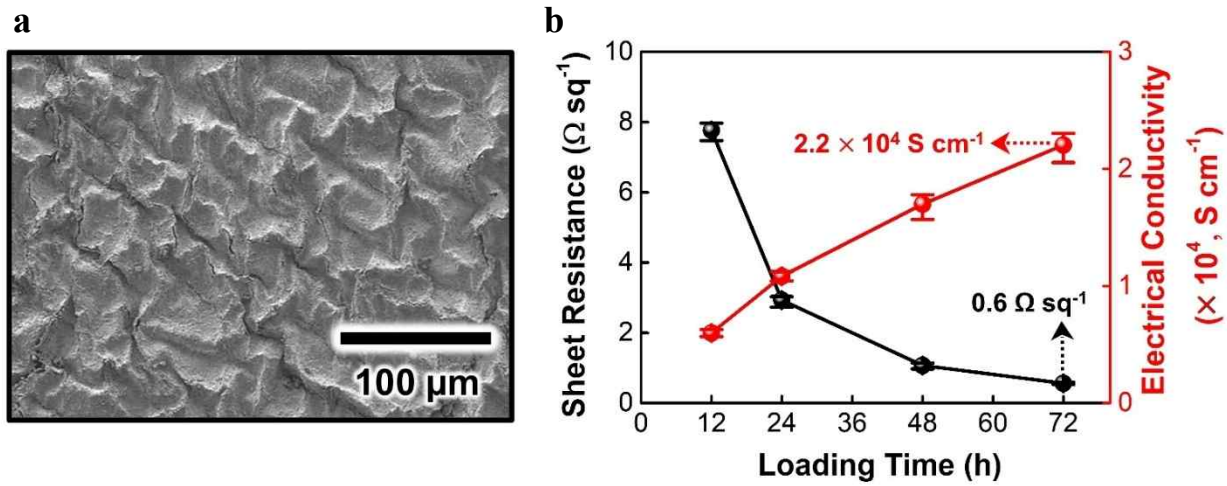

Figure S7. Characterization of TAH-based on PEI ~ 25,000-hydrogel. a) Planar SEM image. b) Sheet resistance and electrical conductivity as a function of loading time.

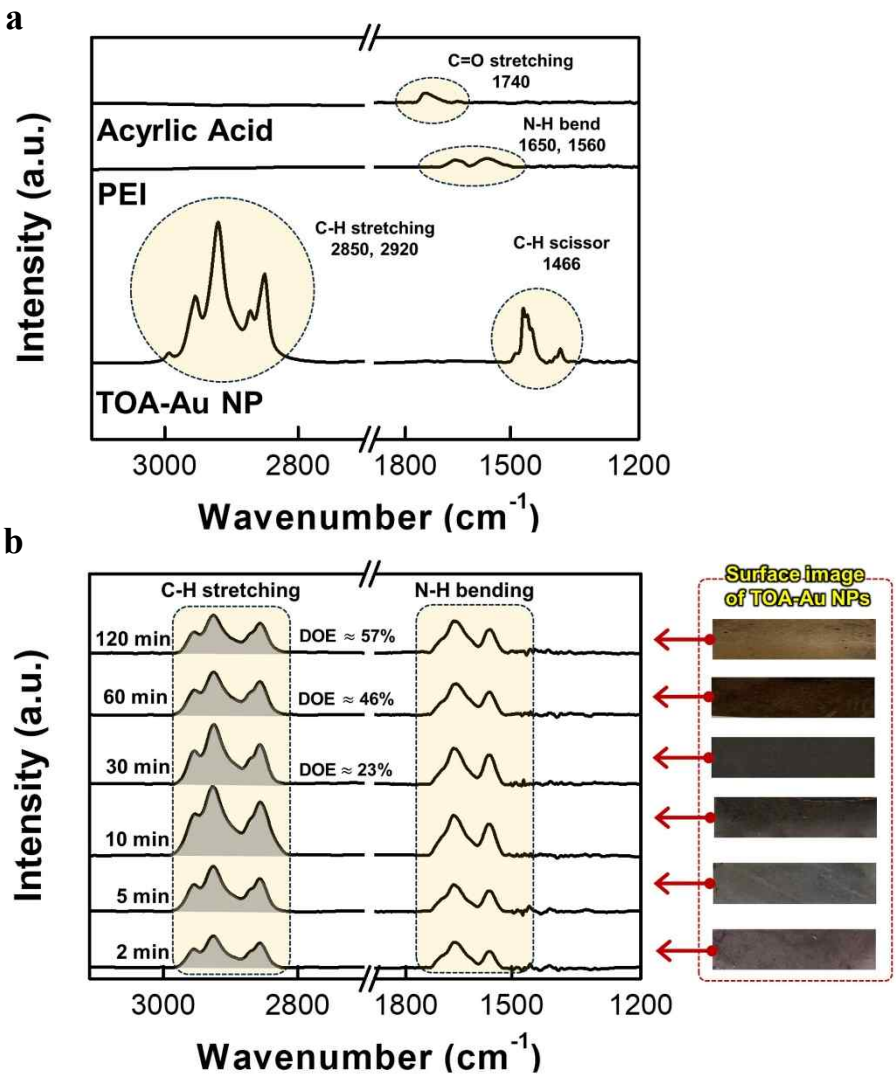

Figure S8. Time-resolved ATR-FTIR analysis of PEI-hydrogel during TOA-Au NP deposition. a) Characteristic FTIR bands associated with each component. b) Time-dependent evolution of FTIR spectra obtained after immersing PEI-hydrogel in TOA-Au NP solution for 2–120 min. The TOA-derived C–H stretching bands reach a maximum at 10 min and subsequently decrease, reflecting TOA-to-PEI ligand exchange. The degree of exchange (DOE), calculated by normalizing the 10-min C–H intensity to 100%, increases from ~23% (30 min) to ~46% (60 min) and ~57% (120 min). The photographs on the right illustrate the gradual deposition of Au onto the hydrogel surface during the TOA-Au NP immersion process.

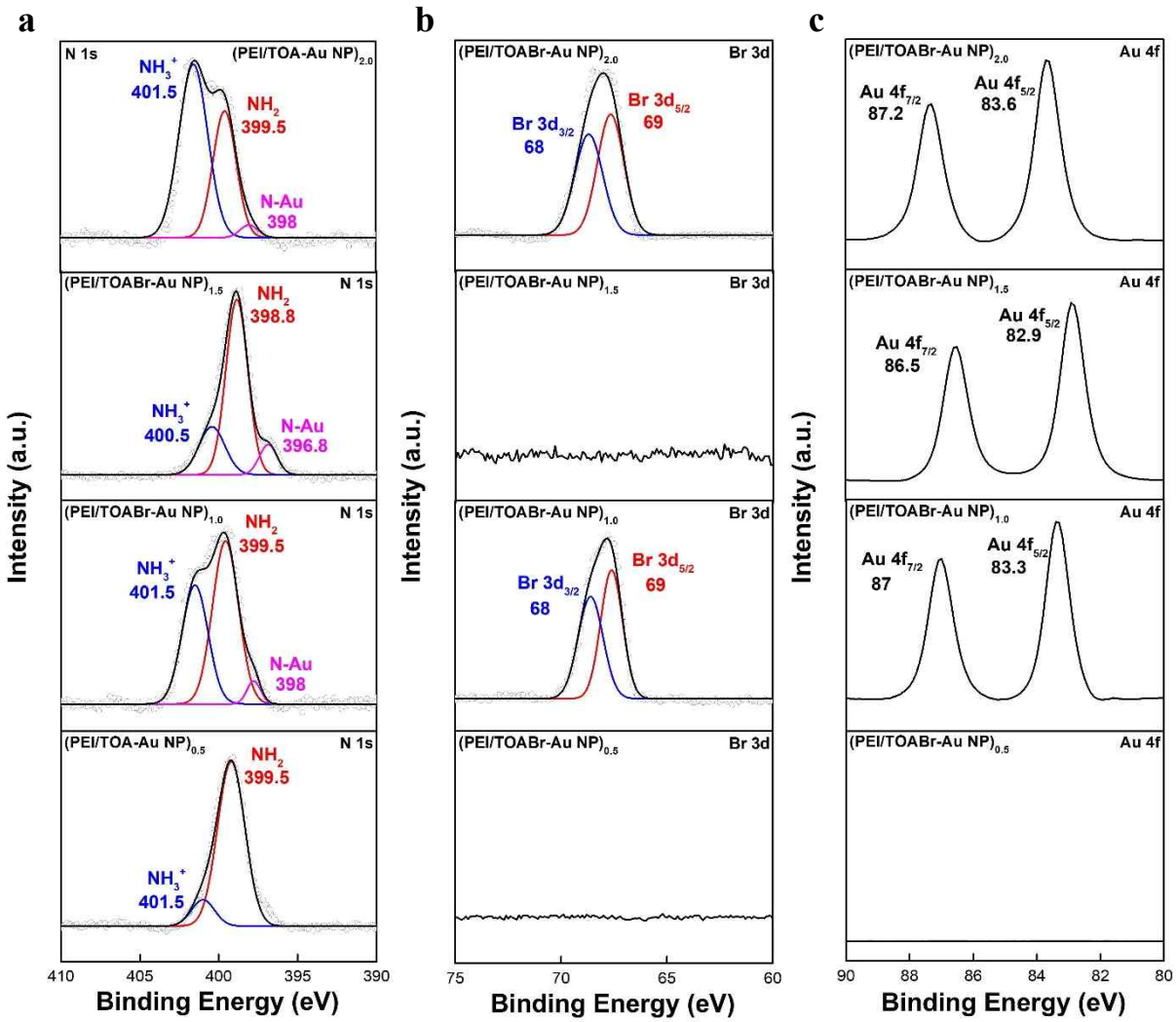

Figure S9. High-resolution XPS spectra of (PEI/TOA-Au NP)$_n$ multilayers. a) N 1s spectra showing the emergence of Au–N coordination (~398 eV) and the reduction of NH_3^+, indicative of progressive ligand exchange between PEI and TOA ligands. b) Br 3d spectra exhibiting systematic attenuation of Br $3d_{5/2}$, Br $3d_{3/2}$ peaks, confirming TOA removal as multilayer assembly proceeds. c) Au 4f spectra demonstrating chemical shifts associated with the transition from TOA-stabilized Au NPs to PEI-coordinated Au nanoplates.

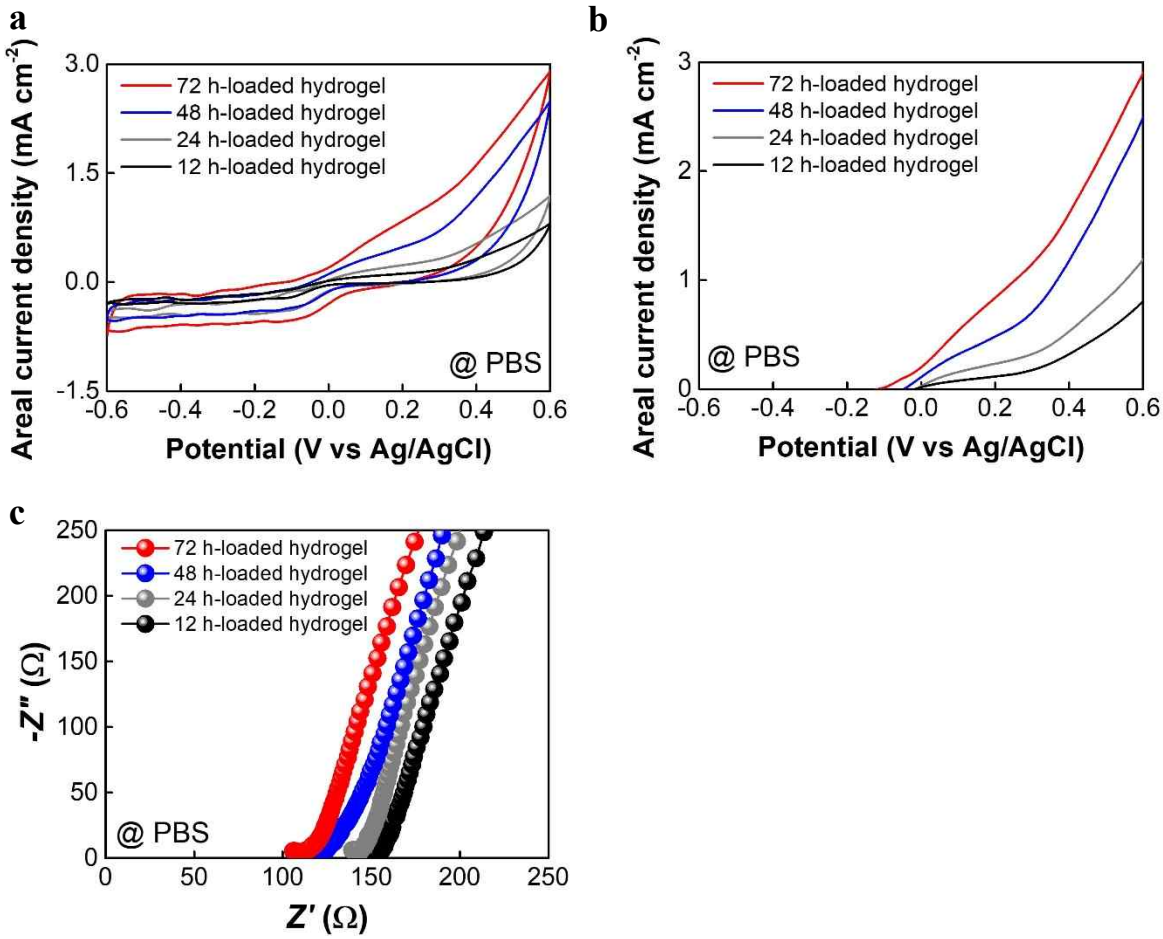

Figure S10. Electrochemical performance of the hydrogel as a function of loading time in the TOA-Au NP solution. a) CV curves of each loading time. b) LSV curves of each loading time. c) Nyquist curves of each loading time (12 h, 24 h, 48 h, and 72 h).

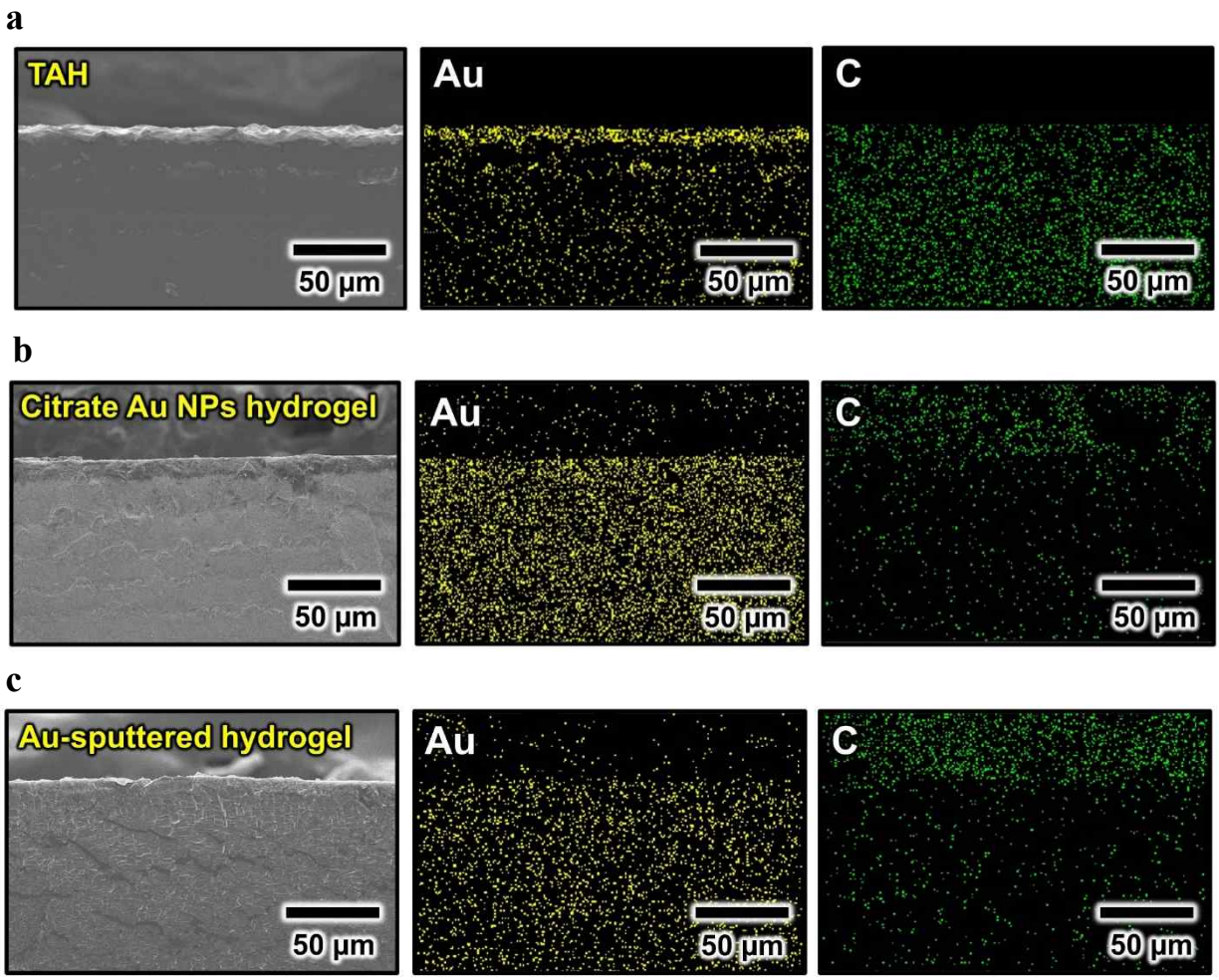

Figure S11. Comparison of FE-SEM cross-sectional images of Au-based hydrogels. Cross-sectional FE-SEM images (left side) and energy-dispersive X-ray spectroscopy (EDX) mapping images (Au and C) of a) TAH, b) citrate Au NPs hydrogel, and c) Au-sputtered hydrogel.

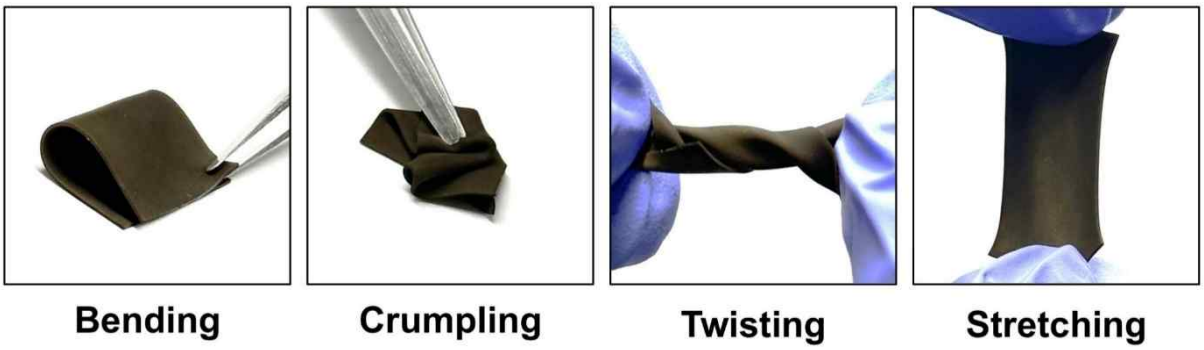

Figure S12. Deformability of flexible hydrogel. Photographic images of deformability of flexible hydrogel, including bending, crumpling, twisting, and stretching.

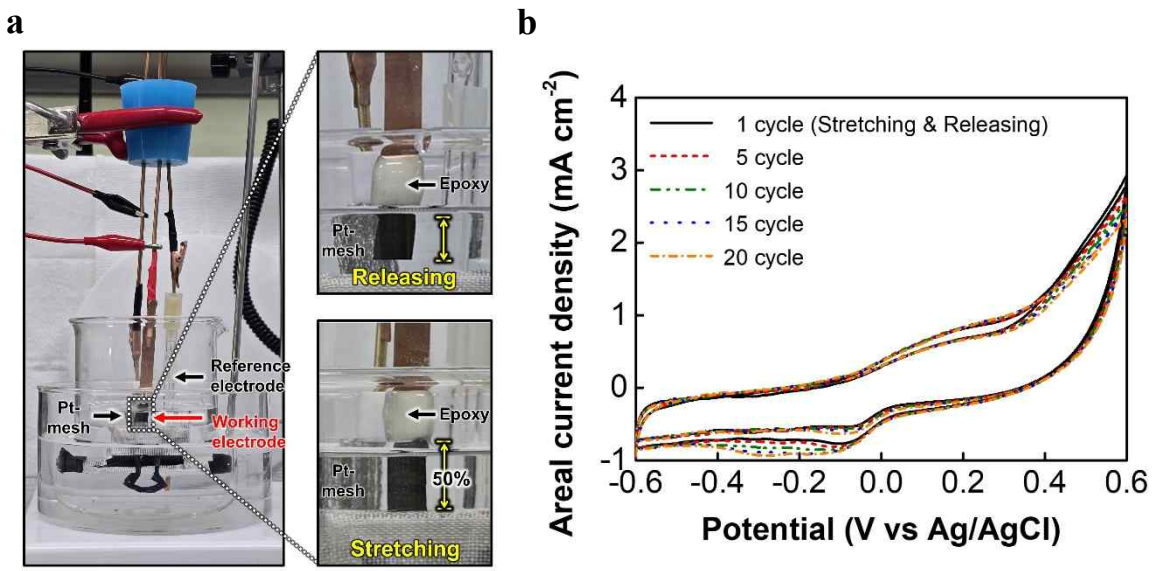

Figure S13. Mechanical–electrochemical performance of the TAH under dynamic stretching. (a) Digital photographs of the TAH integrated into a three-electrode system, shown in the released (0% strain) and stretched (50% strain) states during CV measurements. (b) CV curves recorded during cyclic release–stretch deformation (0% ↔ 50% strain), demonstrating the stable electrochemical response and mechanical robustness of the TAH under dynamic operation.

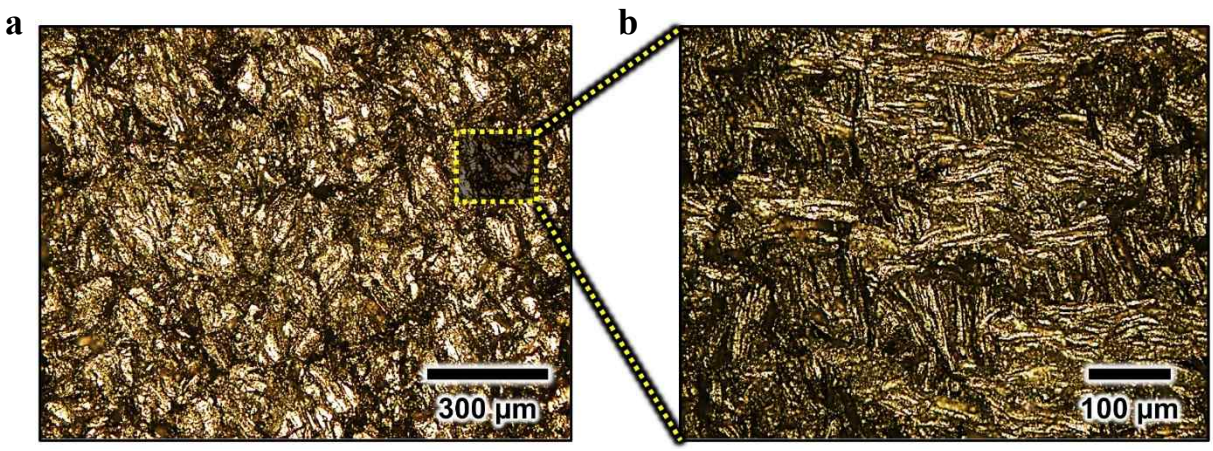

Figure S14. Optical micrographs of TAH. Optical micrographs of a TOA-Au NP coated surface captured at two different magnifications. a) a low-magnification view. b) a high-magnification view. A higher-magnification view highlights the corrugated structural features.

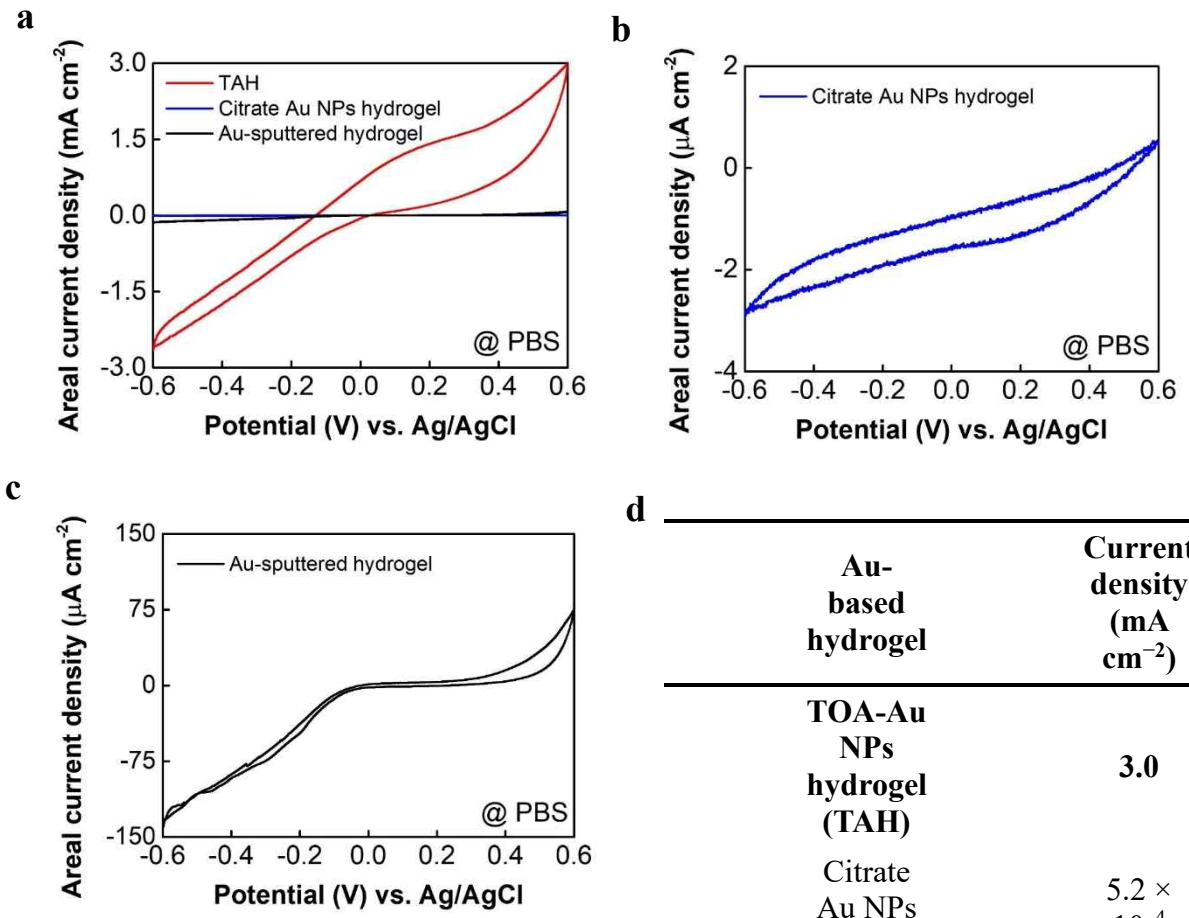

d

Au-based hydrogel	**Current density (mA cm^{-2})**
TOA-Au NPs hydrogel (TAH)	**3.0**
Citrate Au NPs hydrogel	5.2×10^{-4}
Au-sputtered hydrogel	7.5×10^{-2}

Figure S15. CV curves comparing the three types of Au-based hydrogel in PBS solution. a) CV curve of TAH (red), citrate Au NPs hydrogel (blue), and Au-sputtered hydrogel (black). b) CV curve of citrate Au NPs hydrogel. c) CV curve of Au-sputtered hydrogel. d) Summary table of the areal current density of Au-based hydrogels.

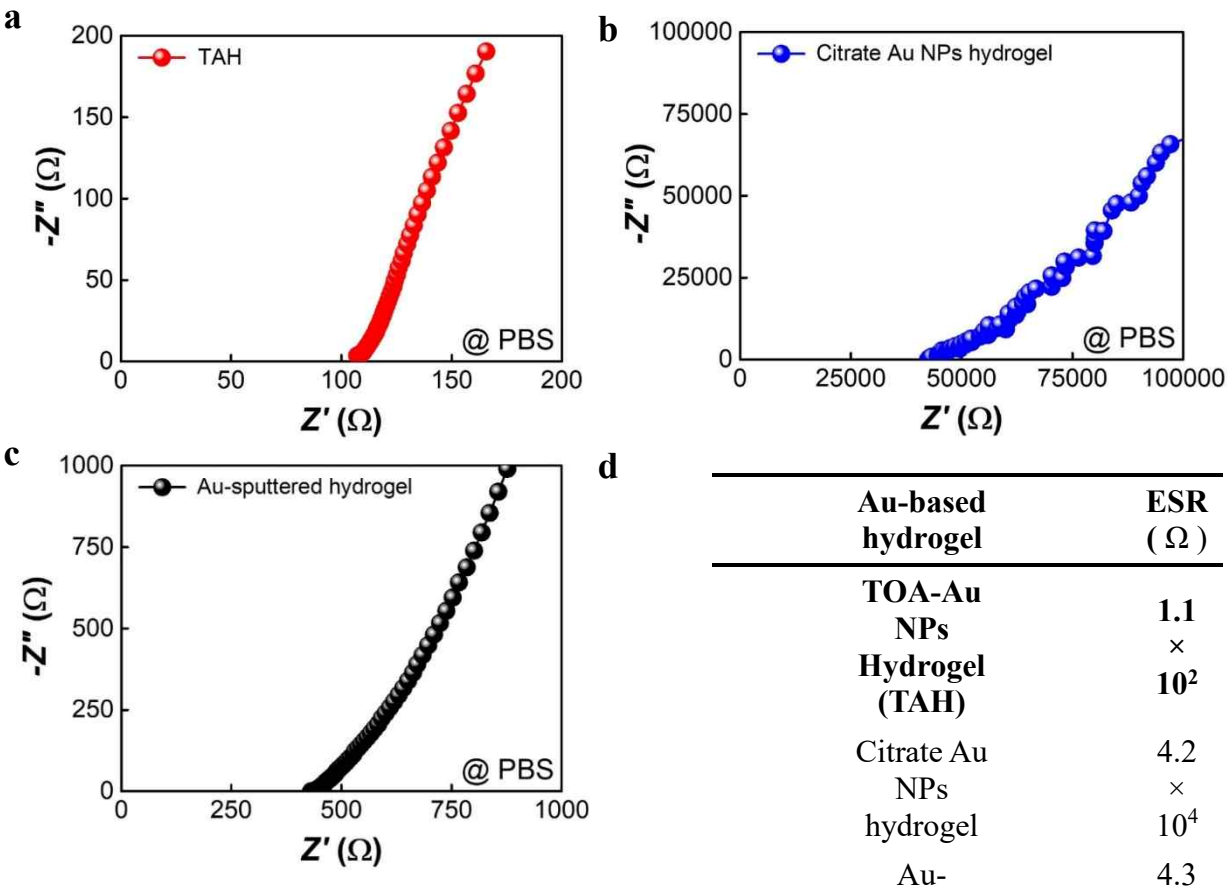

d

Au-based hydrogel	ESR (Ω)
TOA-Au NPs Hydrogel (TAH)	**1.1×10^2**
Citrate Au NPs hydrogel	4.2×10^4
Au-sputtered hydrogel	4.3×10^2

Figure S16. Nyquist plots comparing the three types of Au-based hydrogel in PBS solution. a) Nyquist plot of TAH (red). b) Nyquist plot of citrate Au NPs hydrogel (blue). c) Nyquist plot of Au-sputtered hydrogel (black). d) Summary table of the equivalent series resistance (ESR) of Au-based hydrogels. All measurements were conducted in PBS solution at a scan rate of 5 mV s^{-1}.

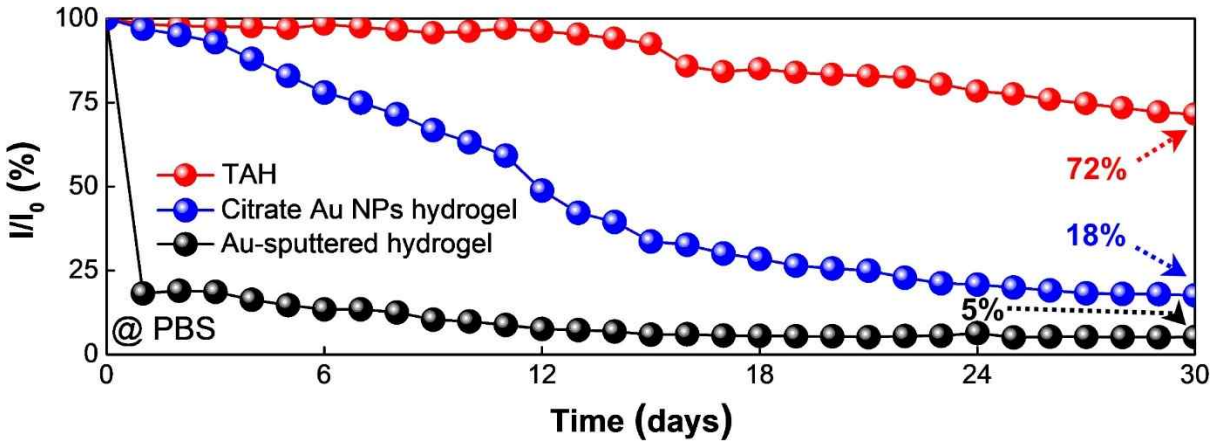

Figure S17. Long-term stability of Au-based hydrogels over 30 days in PBS solution. The TAH (red) shows 72% retention of its initial current density (I_0 = 3.0 mA cm^{-2}, I = 2.1 mA cm^{-2}). The citrate Au NPs hydrogel (blue) exhibits a significant decrease, retaining only 18% of its initial current density (I_0 = 5.2 × 10^{-4} mA cm^{-2}, I = 9.4 × 10^{-5} mA cm^{-2}). The Au-sputtered hydrogel (black) shows the lowest stability, retaining only 5% of its initial current density (I_0 = 7.5 × 10^{-2} mA cm^{-2}, I = 3.8 × 10^{-3} mA cm^{-2}) after 30 days.

Figure S18. Visual observation of the Au-sputtered hydrogel during electrochemical testing in PBS solution.

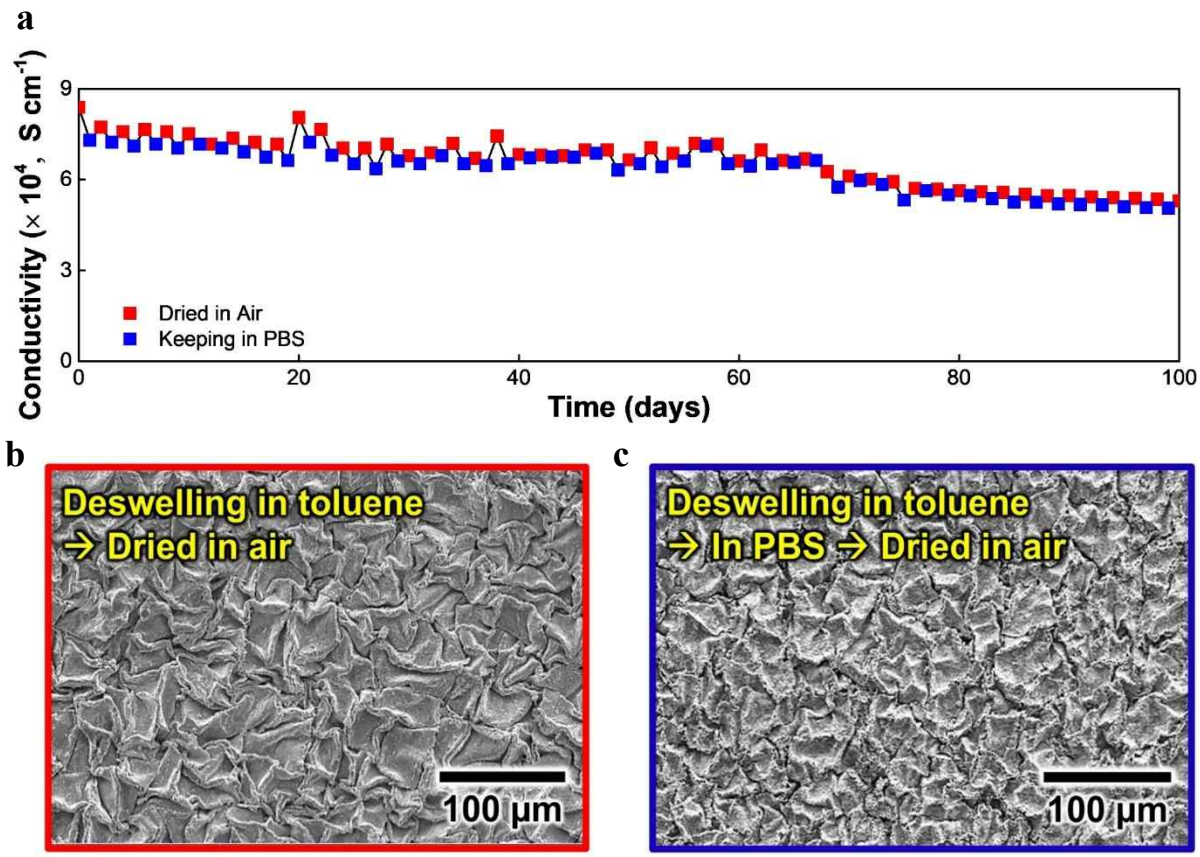

Figure S19. Long-term stability of TAH electrical conductivity. a) Time-dependent electrical conductivity of TAH monitored over 100 days under two different storage conditions. b) dried in air (red) and c) immersed in PBS solution (blue). The SEM images show the surface morphology of the hydrogel after drying in air (red box) and after continuous immersion in PBS solution (blue box).

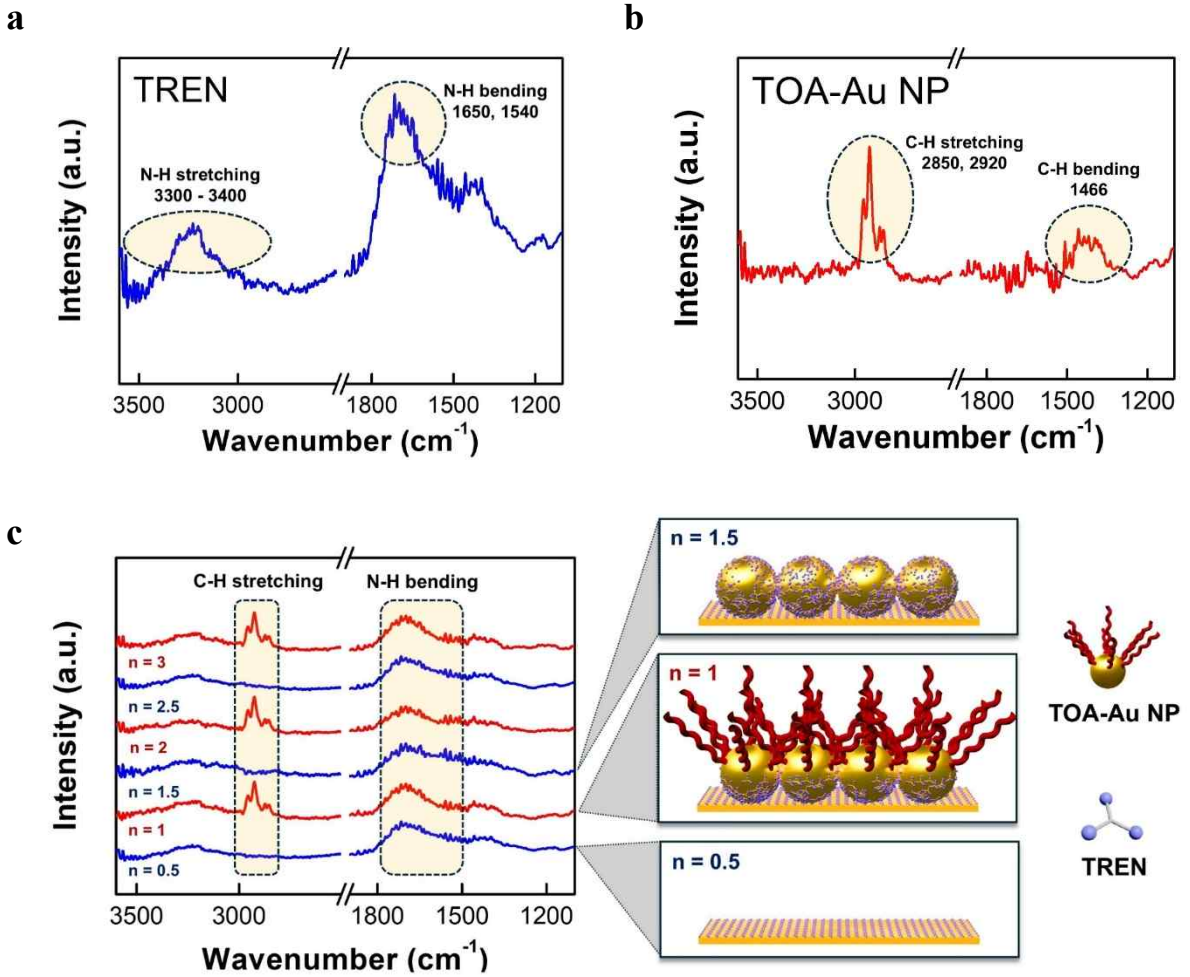

Figure S20. Fourier transform infrared (FTIR) spectra of (TREN/TOA–Au NP)$_n$ multilayers. a) FTIR spectrum of pristine TREN, exhibiting characteristic N–H stretching (3300–3400 cm^{-1}) and N–H bending (1650, 1540 cm^{-1}) peaks. b) FTIR spectrum of pristine TOA–Au NPs, displaying C–H stretching (2850, 2920 cm^{-1}) and C–H bending (1466 cm^{-1}) peaks arising from the long alkyl chains of TOA ligands. c) FTIR spectra of (TREN/TOA–Au NP)$_n$ multilayers, indicating ligand exchange reactions (LER) between TREN and TOA–Au NPs during LbL assembly. At integer bilayer numbers (n = 1, 2, 3), pronounced C–H stretching peaks at 2850 and 2920 cm^{-1} indicate the retention of TOA ligands. In contrast, at half-integer bilayers (n = 0.5, 1.5, 2.5), these C–H peaks nearly disappear, consistent with ligand exchange between the pristine TOA ligands and TREN molecules.

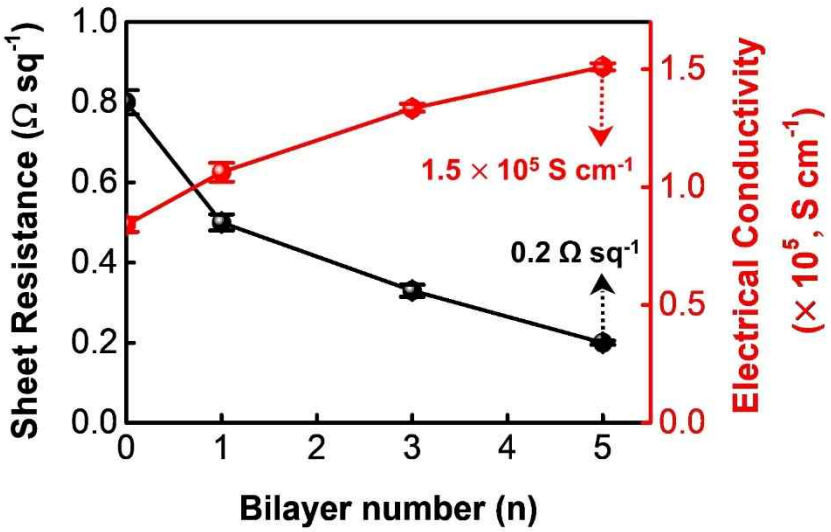

Figure S21. Sheet resistance and electrical conductivity of metallic TOA-Au NPs hydrogel (n-MTAH) assembled with increasing bilayers of (TREN/TOA-Au NP)$_n$ (n = 0, 1, 3, and 5).

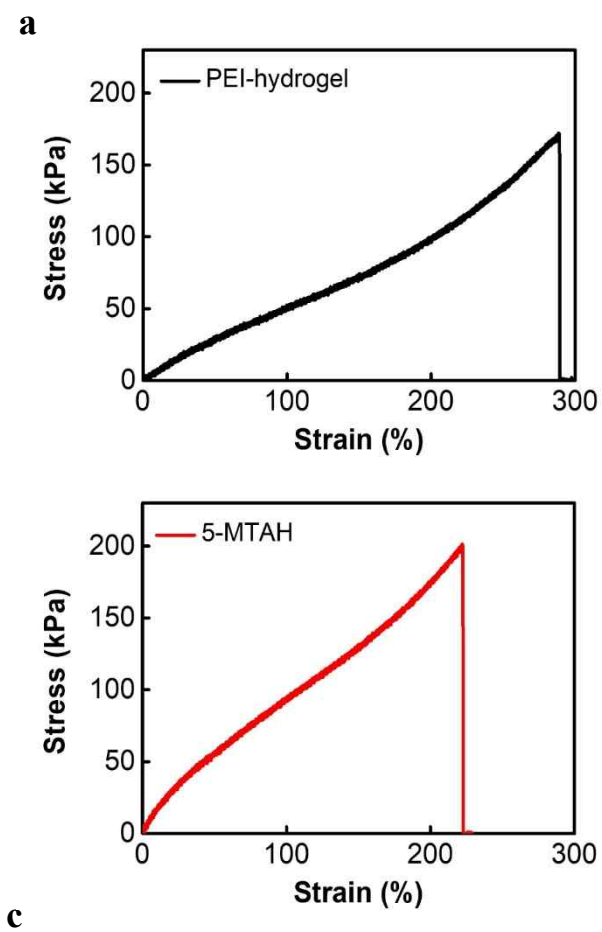

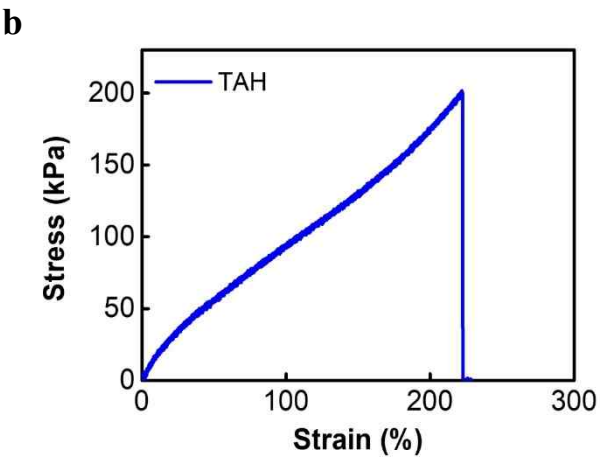

c

d

Hydrogel	Young's modulus (kPa)	Stra (%
PEI-hydrogel	65	289
TAH	181	222
5-MTAH	182	222

Figure S22. Stress–strain curves of a) PEI-hydrogel, b) TAH, and c) 5-MTAH. d) Summary table comparing Young's modulus and maximum strain of the hydrogels.

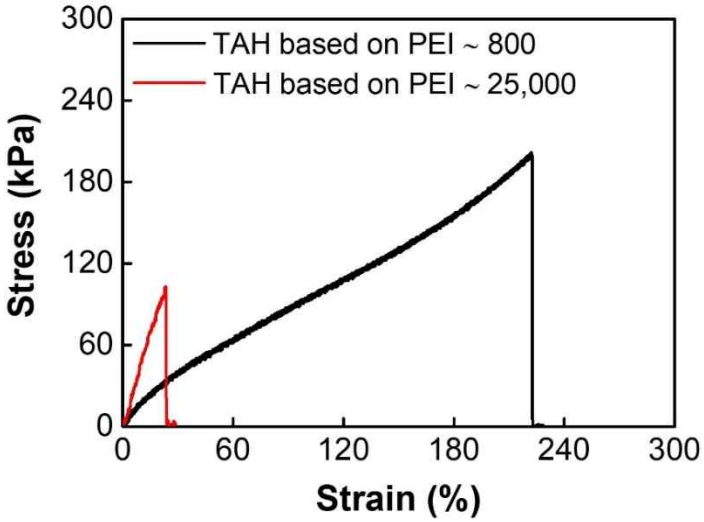

Figure S23. Stress–strain curves of the TAH prepared with PEI (Mw ~ 25,000) compared with those of our PEI (Mw ~ 800) hydrogel.

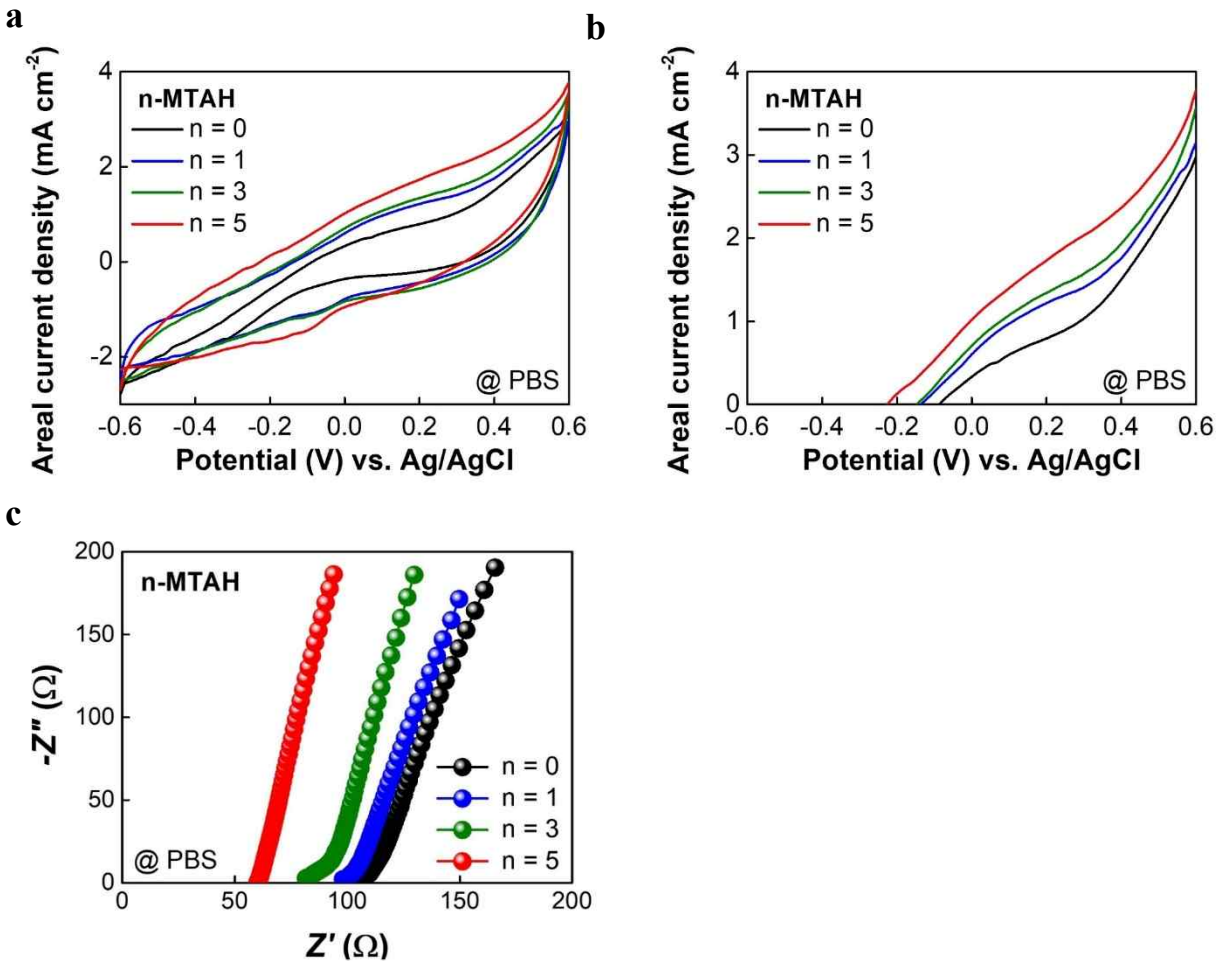

Figure S24. Electrochemical performance of $(TREN/TOA\text{-}Au\ NP)_n$ multilayered assembly on the TAH. a) CV curves and b) areal current densities of $(TREN/TOA\text{-}Au\ NP)_n$ multilayers (n = 0, 1, 3, and 5) on the TAH electrode in PBS solution at a scan rate of 5 mV s^{-1} at 36.5 ℃. c) Nyquist plots of $(TREN/TOA\text{-}Au\ NP)_n$ multilayered assembly on the TAH electrode depending on bilayer number (n). In this case, the ESR values for n = 0, 1, 3, and 5 were approximately 107, 98, 82, and 60 Ω, respectively. Nyquist plots of n-MTAH depending on the bilayer number (n) of $(TREN/TOA\text{-}Au\ NP)_n$ multilayers.

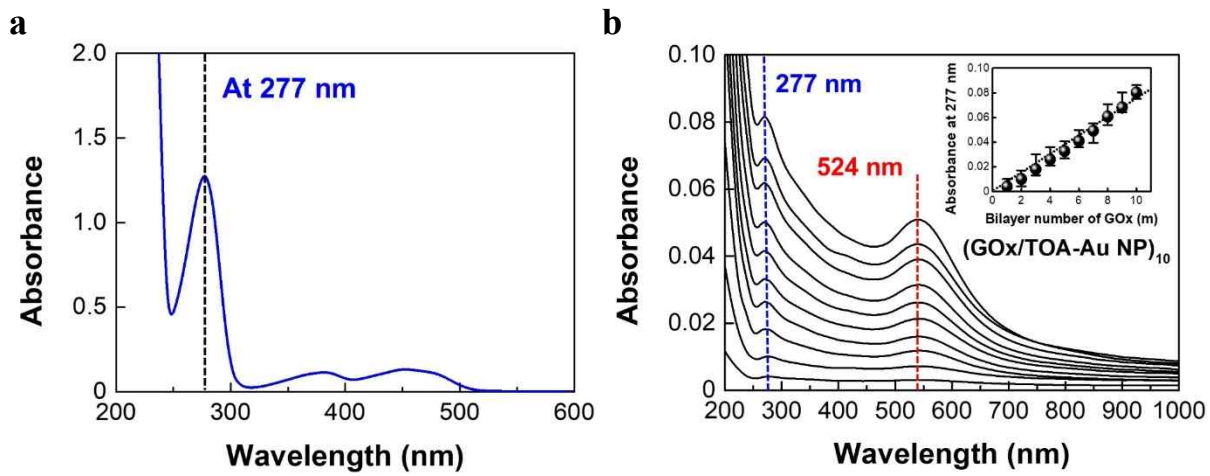

Figure S25. UV-vis spectroscopy. a) UV-vis spectrum of GOx solution with a prominent absorption peak at 277 nm associated with the oxidized flavin cofactor in GOx.[S6] b) $(GOx/TOA\text{-}Au\ NP)_m$ multilayers. The inset shows hyperchromicity of the multilayers at 277 nm.

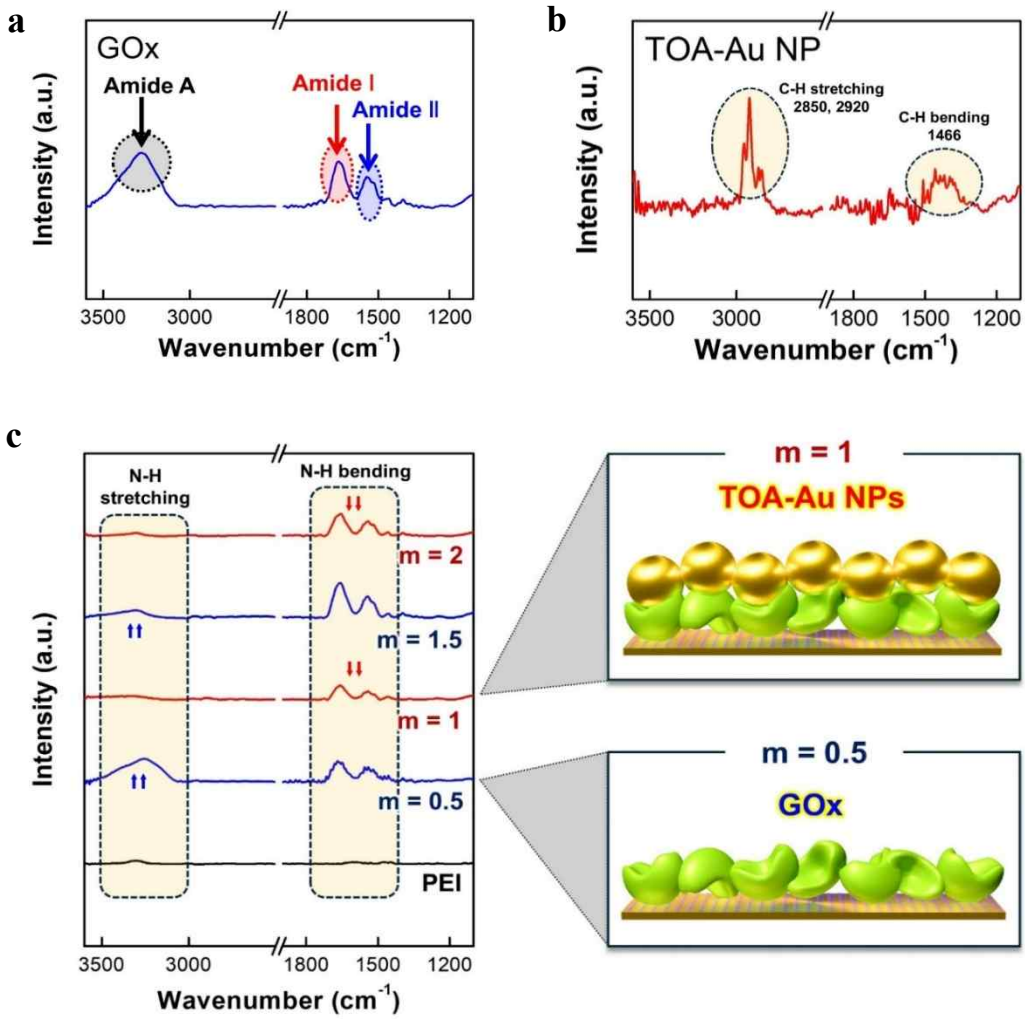

Figure S26. FTIR spectra of $(GOx/TOA\text{-}Au\ NPs)_m$ bilayers. a) FTIR spectrum of GOx showing characteristic amide A (3280 cm^{-1}), amide I (1666 cm^{-1}) and amide II (1549 cm^{-1}) bands.[S7,S8] b) FTIR spectrum of TOA-Au NPs exhibiting absorbance peaks at 2850 cm^{-1} and 2920 cm^{-1} from C–H stretching and at 1466 cm^{-1} from C–H bending of the long alkyl chains in TOA ligands. c) FTIR spectra and schematic illustration of $(GOx/TOA\text{-}Au\ NPs)_m$ multilayers as a function of bilayer number. The N–H stretching peaks (at 3280 cm^{-1}) originating from amide A are prominent at half-integer bilayer number (m = 0.5 and 1.5), whereas their intensity markedly decreases at integer bilayer number (m = 1 and 2). These results imply the ligand exchange reaction between pristine TOA ligands (bound to the Au NP surface) and amino acid groups (particularly, amine moieties of amino acid groups) of GOx.

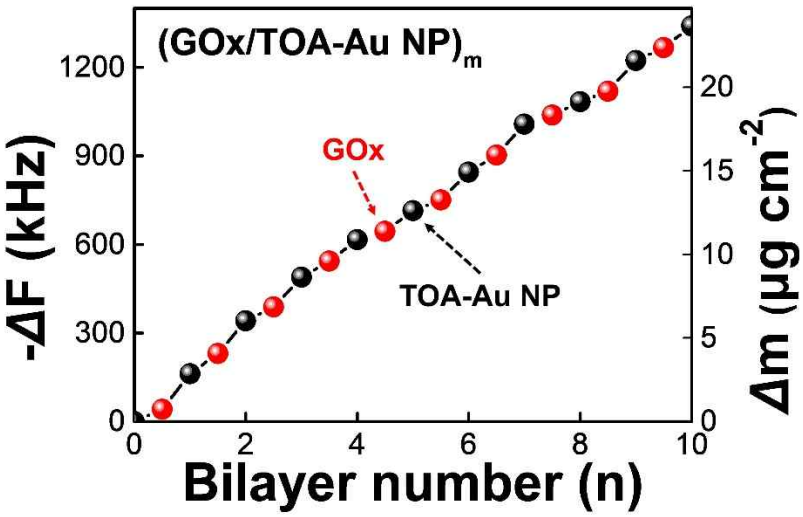

Figure S27. Frequency shift (–ΔF) and the corresponding adsorbed mass (Δm) measured during the sequential LbL assembly of GOx (red) and TOA-Au NP (black) for bilayer numbers m = 0~10.

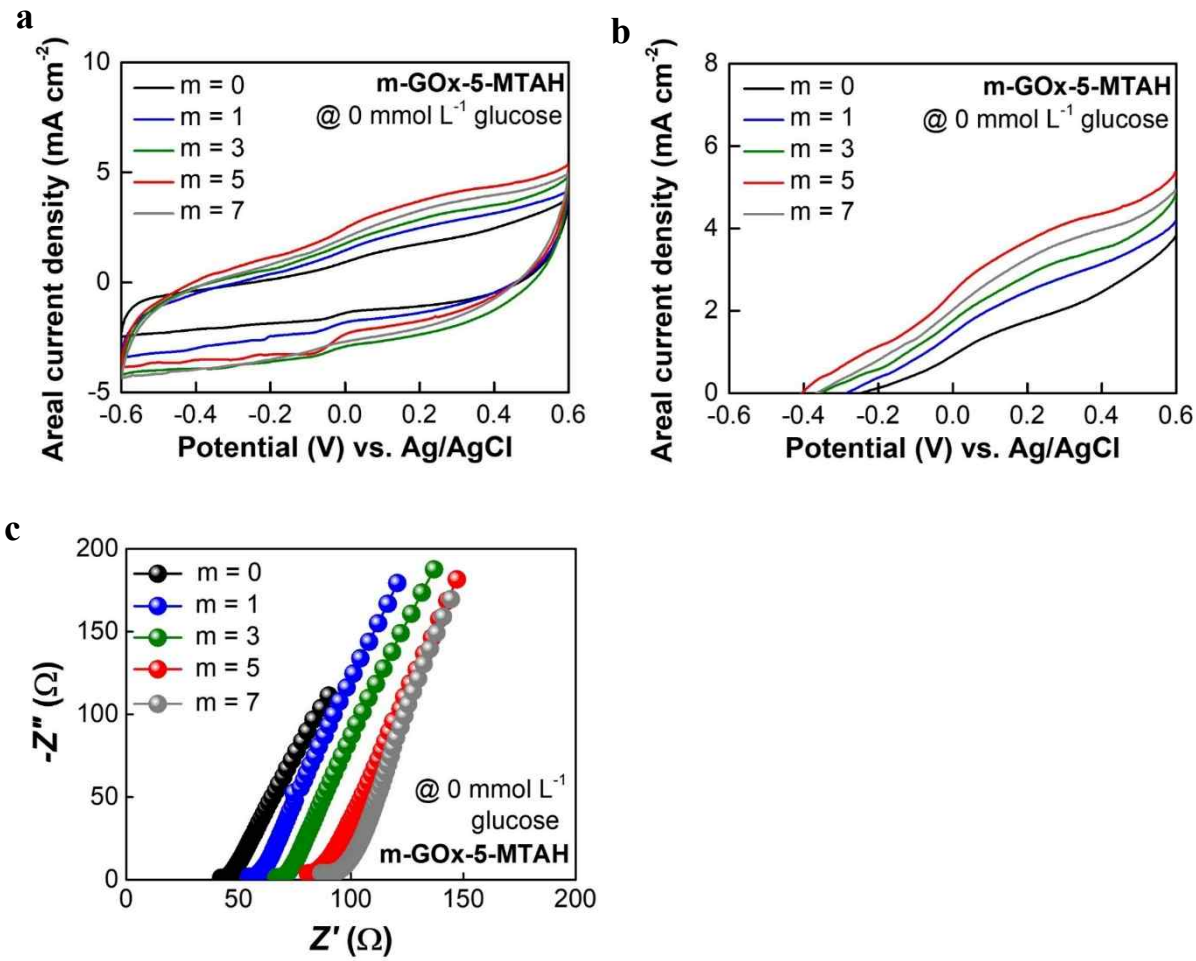

Figure S28. Electrochemical performance of m-GOx-5-MTAH in PBS solution without glucose. a) CV curves of $(GOx/TOA\text{-}Au\ NP)_m$ layers at a scan rate of 5 mV s^{-1} at 36.5 °C for varying bilayer numbers (m). b) Areal current densities of m-GOx-5-MTAH layers at a scan rate of 5 mV s^{-1} in PBS without glucose for varying m. c) Nyquist plots of m-GOx-5-MTAH depending on the bilayer number (m).

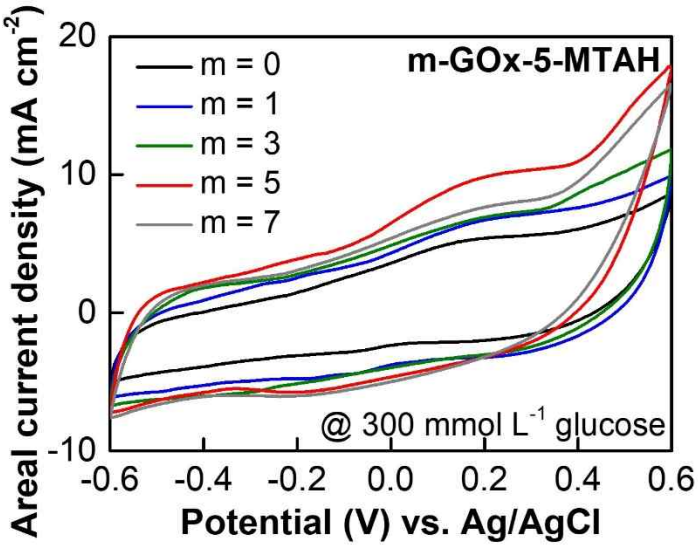

Figure S29. CV curves of m-GOx-5-MTAH in PBS solution containing 300 mmol L^{-1} glucose. CV curve of m-GOx-5-MTAH modified with $(GOx/TOA\text{-}Au\ NP)_m$ (m = 0, 1, 3, 5, and 7) in the presence of 300 mmol L^{-1} glucose at 36.5 °C.

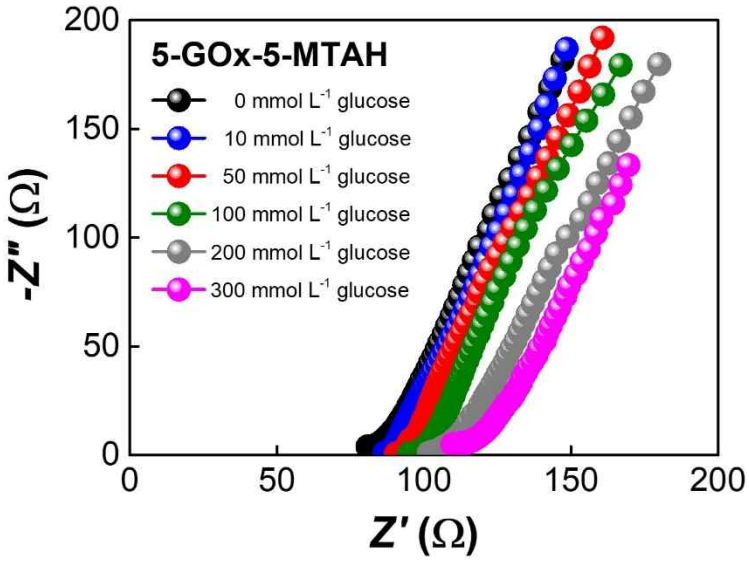

Figure S30. Nyquist plots of 5-GOx-5-MTAH in PBS solution with varying glucose concentrations (0–300 mmol L^{-1} glucose).

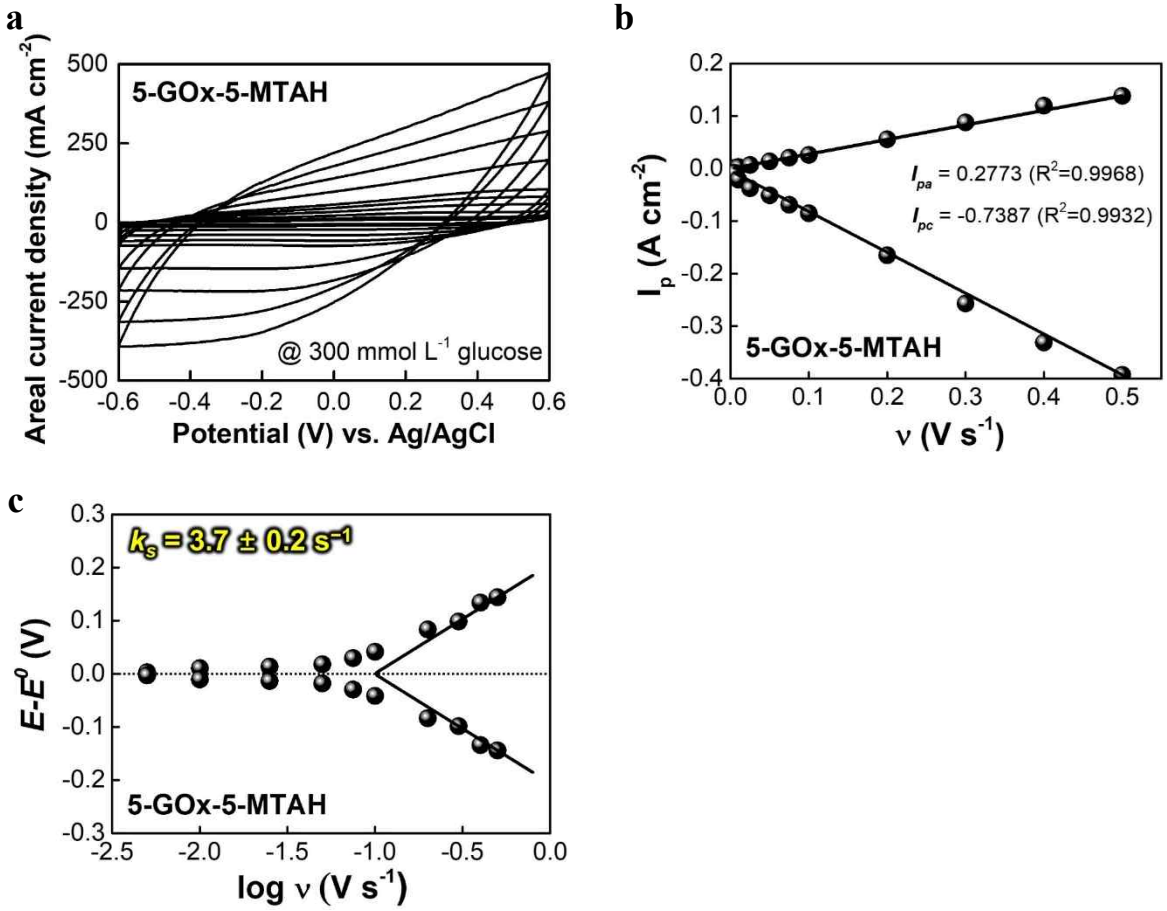

Figure S31. Electrochemical response of the 5-GOx-5-MTAH. a) Scan rate dependent CV curves of 5-GOx-5-MTAH in PBS solution containing 300 mmol L^{-1} glucose. b) Change in the peak current of 5-GOx-5-MTAH with increasing the scan rate (ν) from 0.005 to 0.5 V s^{-1}. c) Change in the potential ($E–E^0$) of 5-GOx-5-MTAH as a function of log (ν).

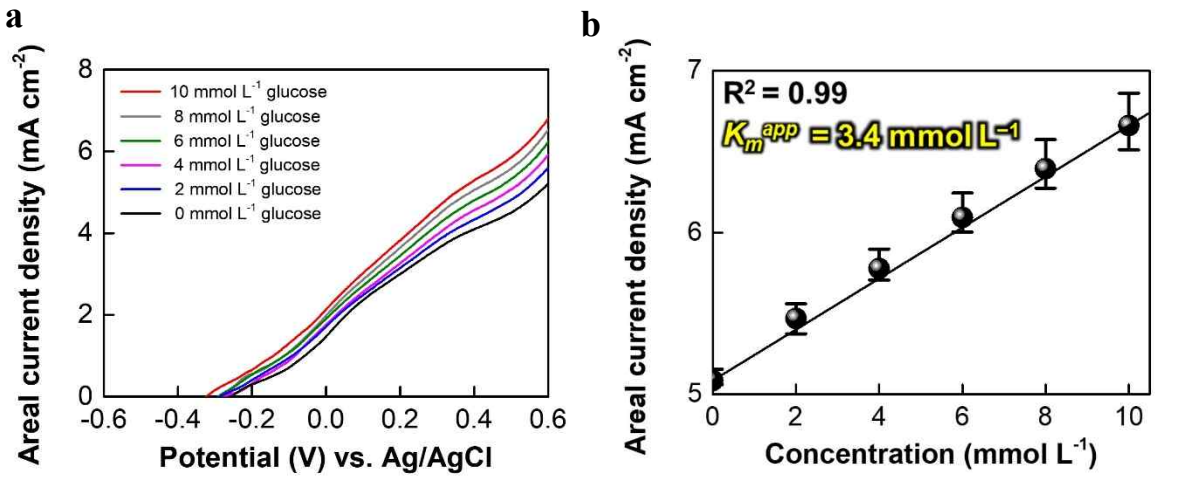

Figure S32. Michaelis–Menten analysis of the 5-GOx-5-MTAH anode. a) LSV curves recorded at low glucose concentrations of 0, 2, 4, 6, 8, and 10 mmol L^{-1}. b) Lineweaver–Burk plot constructed from the current responses obtained at these glucose concentrations.

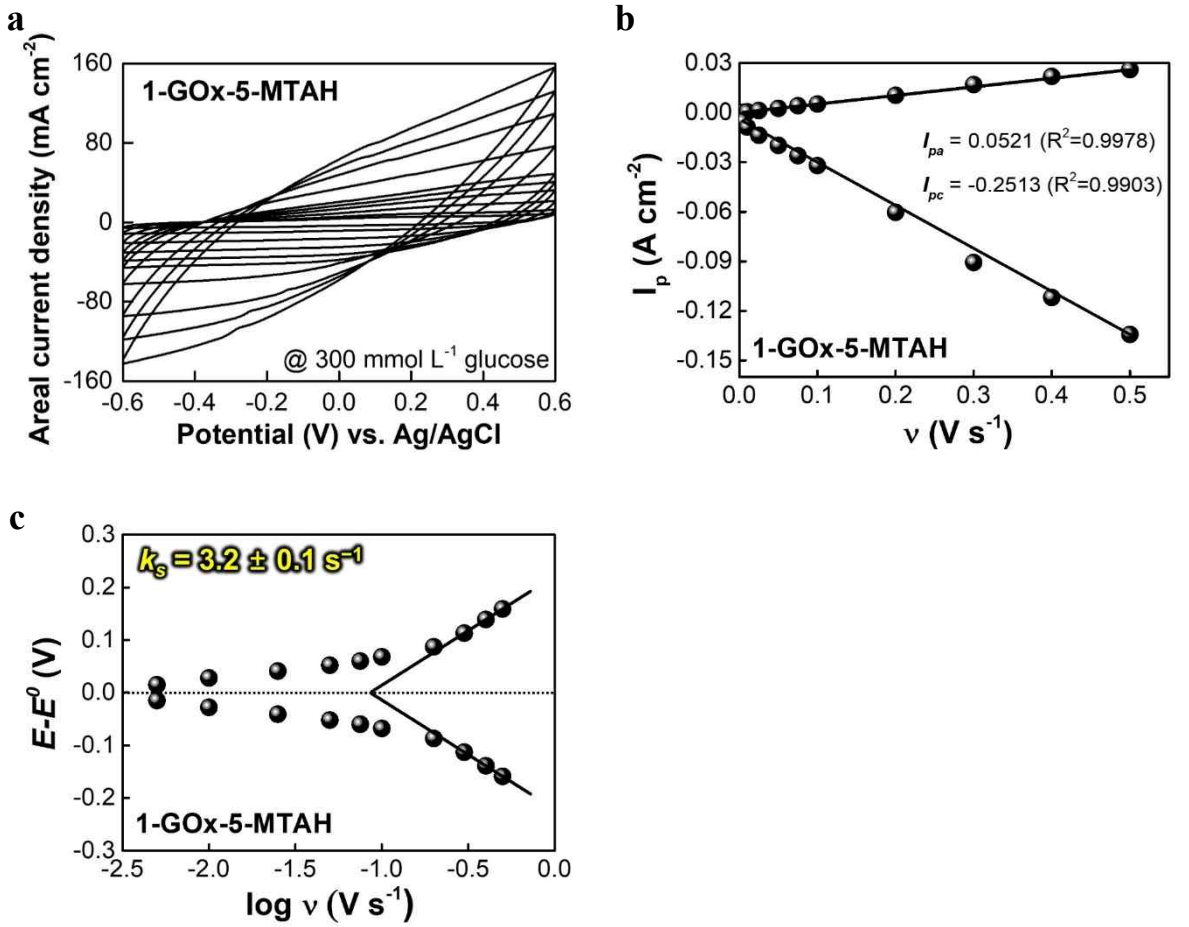

Figure S33. Electrochemical response of the 1-GOx-5-MTAH. a) Scan rate dependent CV curves of 1-GOx-5-MTAH in PBS solution containing 300 mmol L^{-1} glucose. b) Change in the peak current of 1-GOx-5-MTAH with increasing the scan rate (ν) from 0.005 to 0.5 V s^{-1}. c) Change in the potential ($E-E^0$) of 1-GOx-5-MTAH as a function of log (ν).

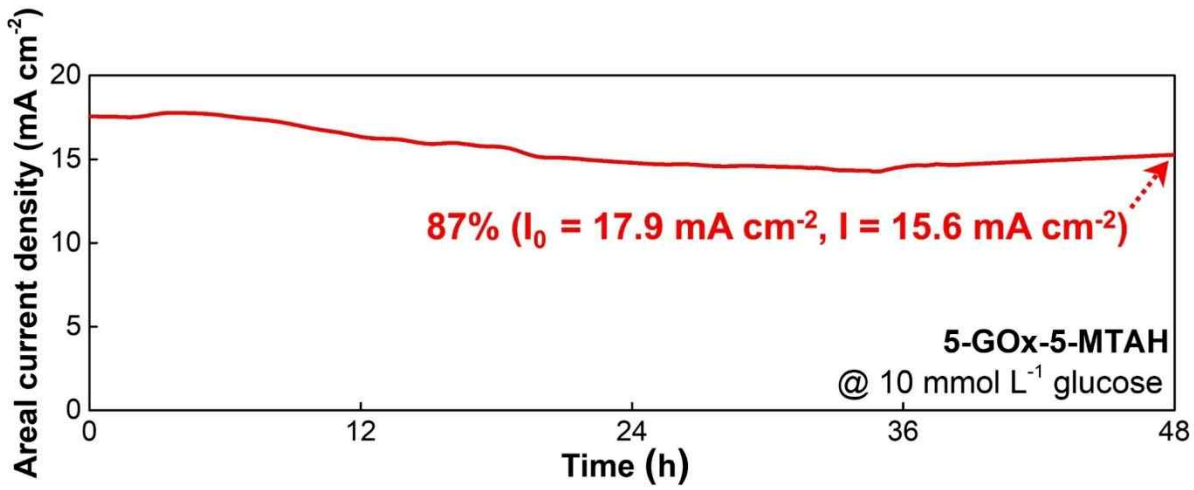

Figure S34. Long-term operational stability of 5-GOx-5-MTAH over 48 h in 10 mmol L^{-1} glucose. The 5-GOx-5-MTAH retained 87% of its initial current density after 48 h of continuous operation, demonstrating excellent operational stability and sustained electrocatalytic activity under 10 mmol L^{-1} glucose.

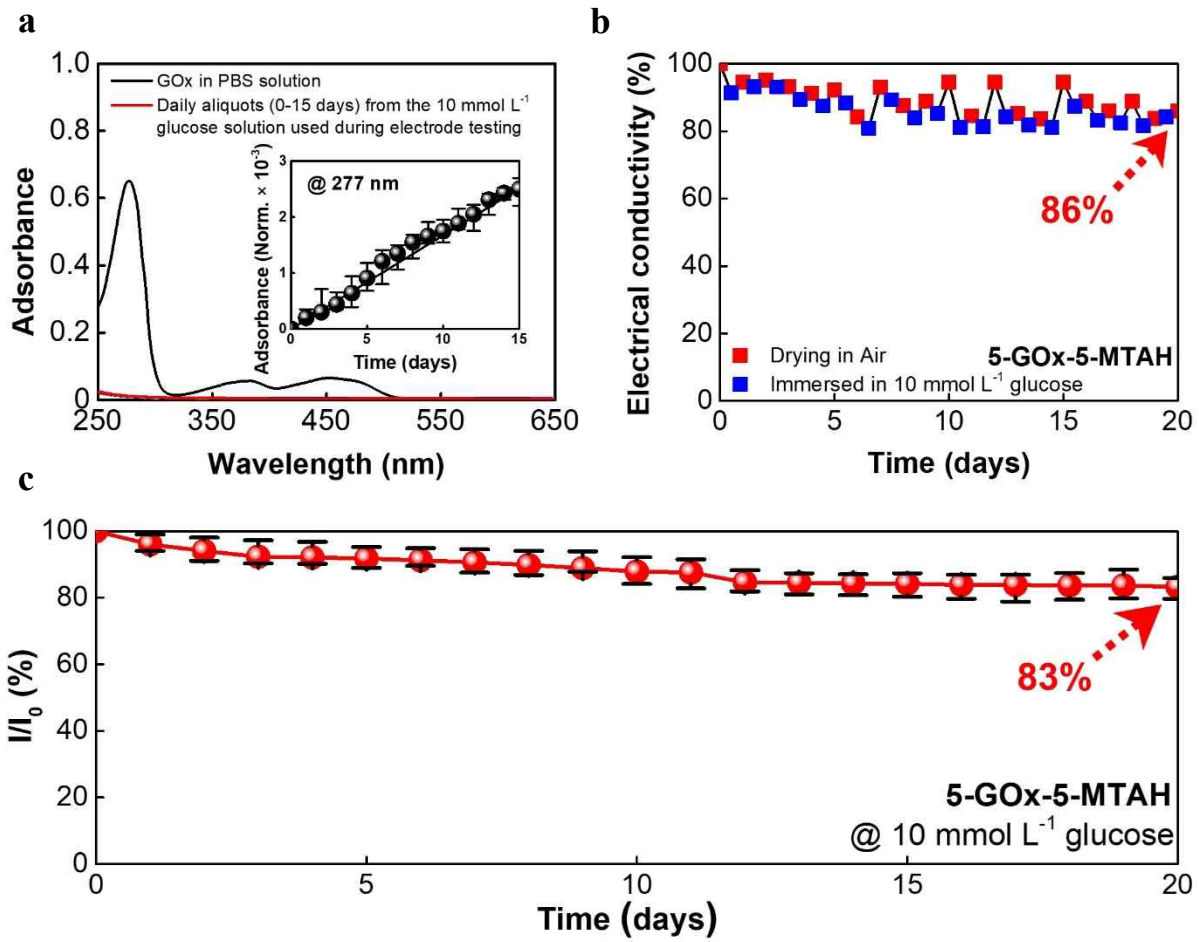

Figure S35. Long-term stability and enzyme-leaching behavior of 5-GOx-5-MTAH. a) UV–vis spectra of GOx in PBS (black) and daily aliquots (0–15 days) of PBS containing 10 mmol L^{-1} glucose used for electrochemical measurements (red), indicating negligible enzyme leaching, as further confirmed by the time-dependent normalized absorbance at 277 nm shown in the inset. b) Electrical conductivity retention of 5-GOx-5-MTAH over 20 days under two different conditions: dried in air (red) and immersed in PBS containing 10 mmol L^{-1} glucose (blue). c) Long-term stability of 5-GOx-5-MTAH in PBS containing 10 mmol L^{-1} glucose over 20 days.

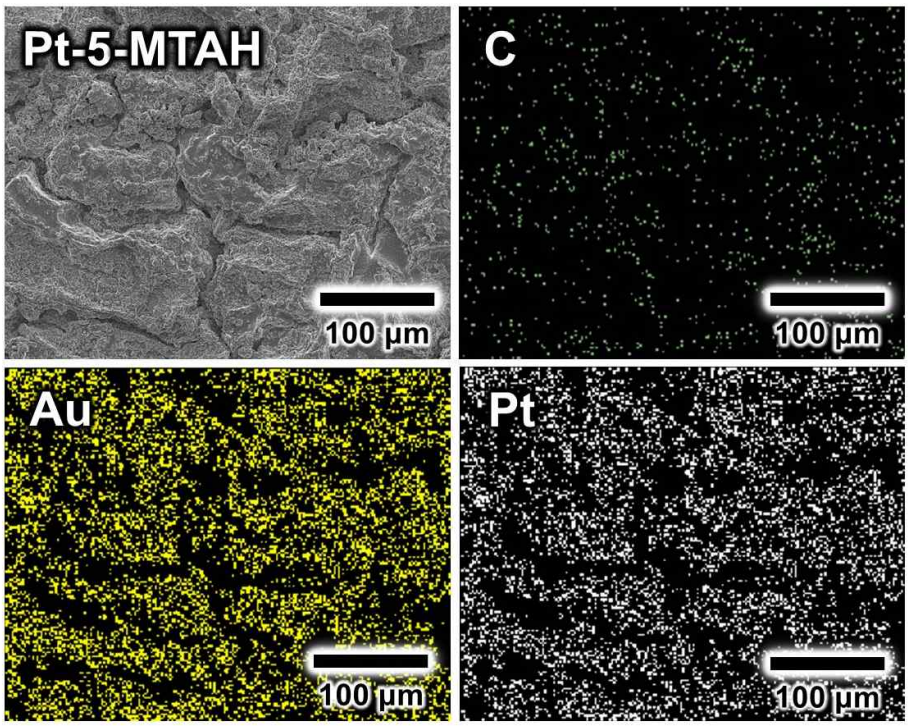

Figure S36. Surface morphology and elemental analysis of the cathode. Planar-view FE-SEM and EDX mapping images of Pt-5-MTAH, showing the elemental distribution of C, Au, and Pt on the electrode surface.

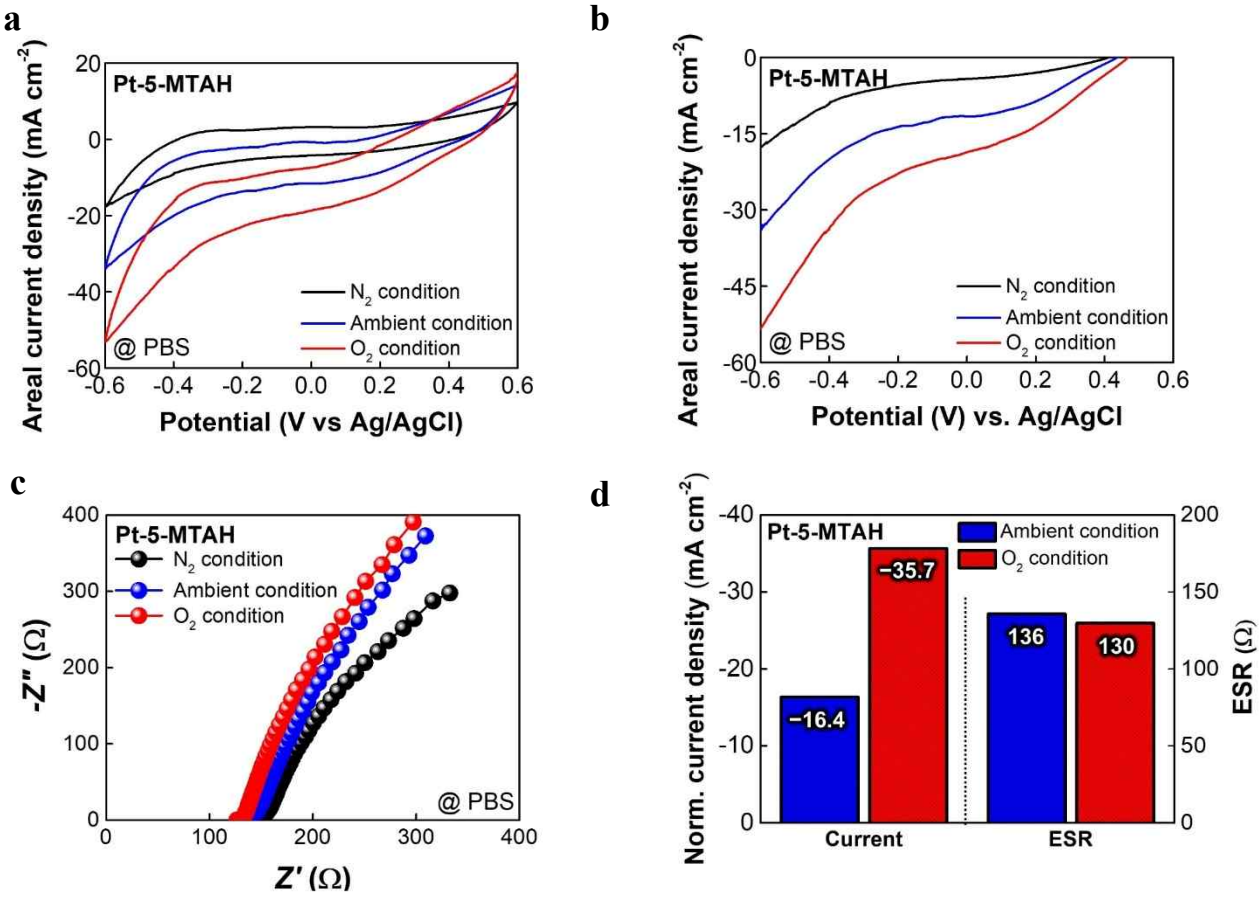

Figure S37. Electrochemical performance of Pt-5-MTAH under three different gas conditions. a) CV curves of the Pt-5-MTAH in PBS solution under N_2-saturated condition, ambient condition, O_2-saturated condition. b) Areal current densities of Pt-5-MTAH in PBS solution under N_2-saturated condition, ambient condition, O_2-saturated condition. c) Nyquist plots of Pt-5-MTAH in PBS solution under N_2-saturated condition, ambient condition, O_2-saturated condition. d) Comparison of normalized current density and ESR under ambient and O_2-saturated condition, referenced to the N_2-saturated condition.

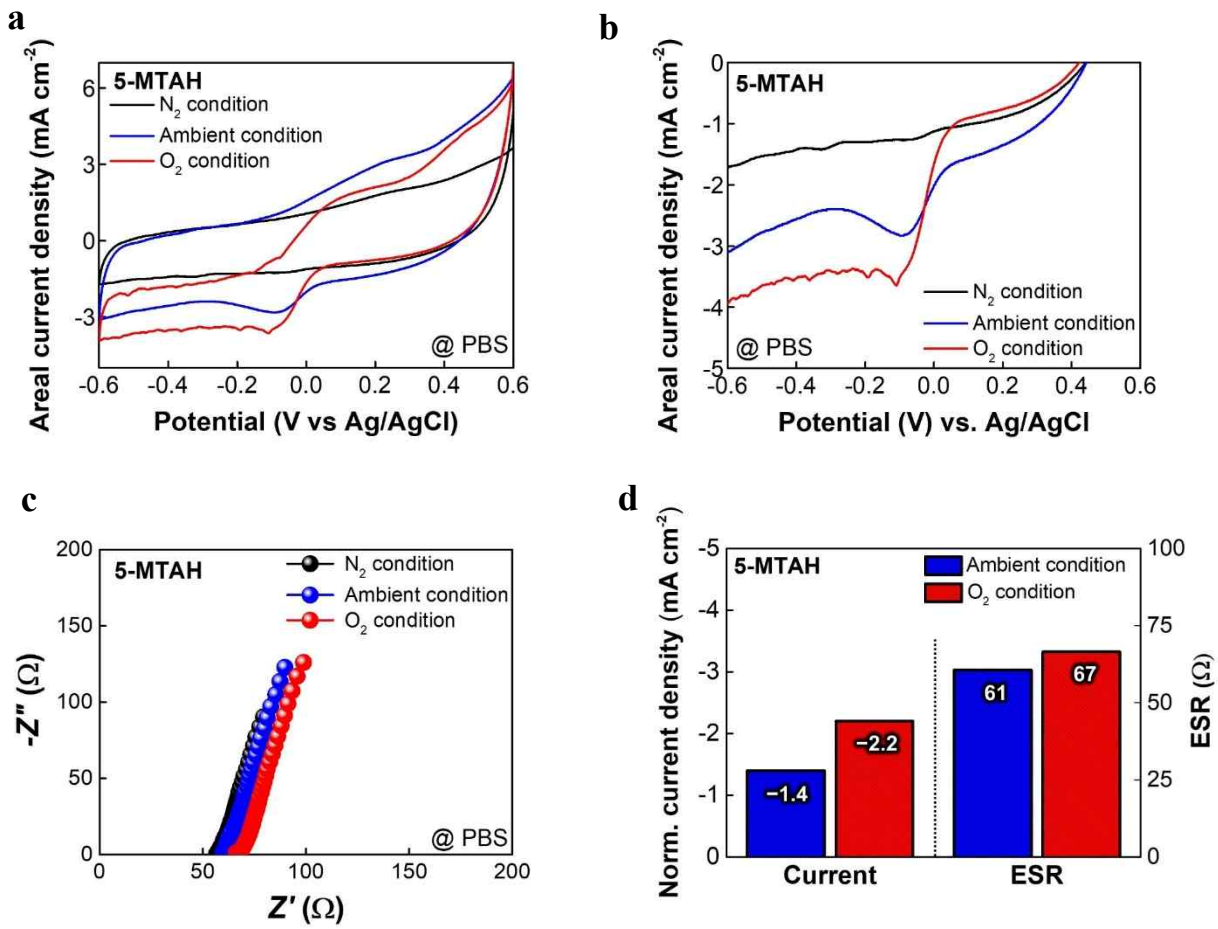

Figure S38. Electrochemical performance of 5-MTAH under three different gas conditions. a) CV curves of 5-MTAH in PBS solution under N_2-saturated condition, ambient condition, O_2-saturated condition. b) Areal current densities of 5-MTAH in PBS solution under N_2-saturated condition, ambient condition, O_2-saturated condition. c) Nyquist plots of 5-MTAH in PBS solution under N_2-saturated condition, ambient condition, O_2-saturated condition. d) Comparison of normalized current density and ESR under ambient and O_2-saturated conditions.

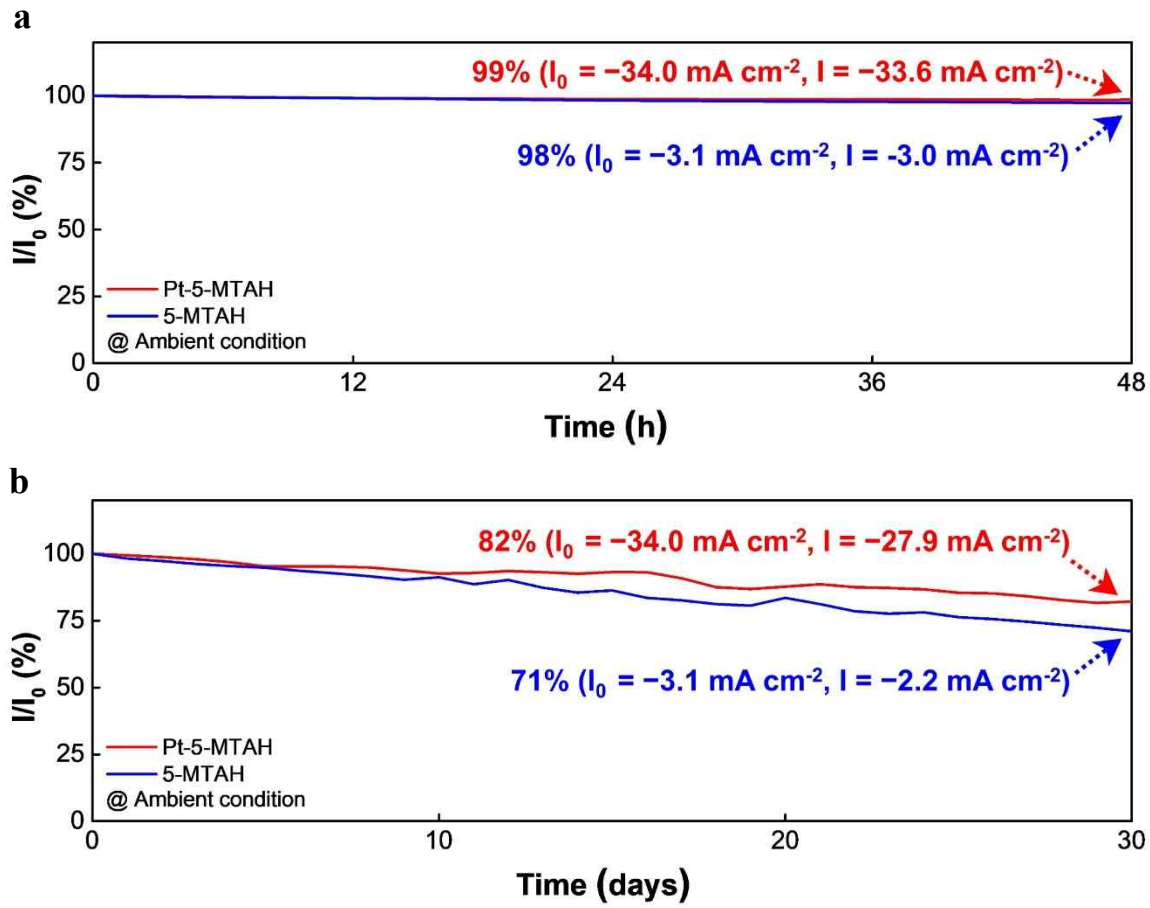

Figure S39. Long-term stability of Pt-5-MTAH (red lines) and 5-MTAH cathode (blue lines) over a) 48 h and b) 30 days in PBS solution under ambient conditions.

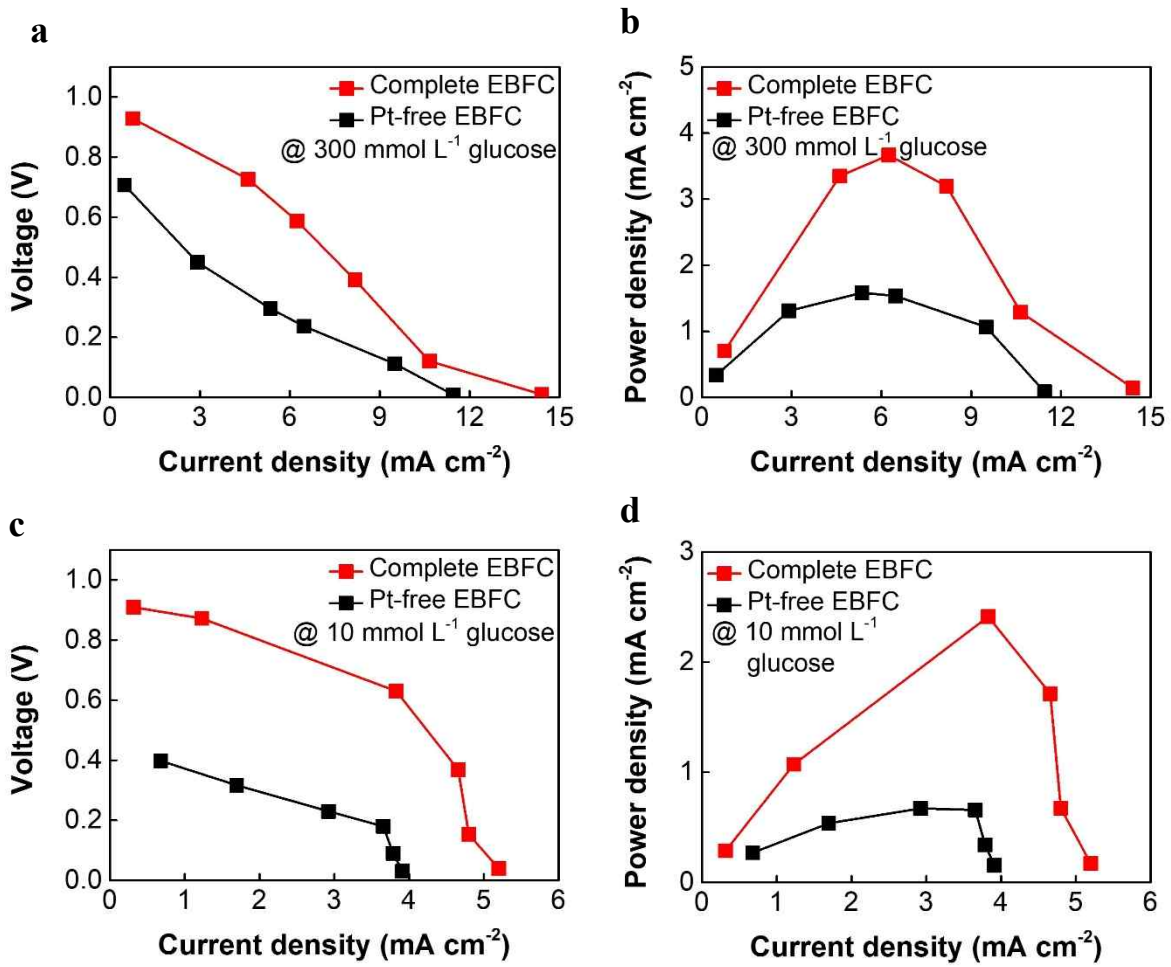

Figure S40. Polarization and power density curves of the complete and Pt-free EBFC measured in PBS solution containing 300 and 10 mmol L^{-1} glucose. a) Voltage (V) − current (I) profile and b) Power (P) − current (I) profile of the EBFC measured in 300 mmol L^{-1} glucose. c) Voltage (V) − current (I) profile and d) Power (P) − current (I) profile of the EBFC measured in 10 mmol L^{-1} glucose. All measurements were conducted under ambient conditions (at 36.5 ℃).

Table S1. Comparison of electrical conductivity in hydrogel electrodes made from different materials.

Materials	Electrical Conductivity (S cm^{-1})	Other Properties	Ref.
Ion-embeded hydrogel			
PAAm (NaCl)	1.0×10^{-3} ~ 5.0×10^{-1}	- Modulus ~ 100 kPa - Stretchability > 1000% - Transparency ~ 98.9%	52
Trehalose-modified PAAm	3.2×10^{-3}	- Modulus ~ 365 kPa - Stretchability ~ 2520% - Toughness ~ 5116 J m^{-2} - Self-healing	51
Bentonite incorporated cellulosic hydrogel	8.9×10^{-2}	- Modulus ~ 3.56 MPa - Stretchability ~ 50% - Toughness ~ 0.45 MJ m^{-3} - Freezing tolerant	54
PAM-AMPS (NaCl)	8.6×10^{-2}	- Modulus ~ 2 kPa -	53

		Stretchability ~ 2902%	
Conductive polymers-incorporated hydrogel			
PEDOT:PSS/PU biphase	> 1.1×10^{1}	- Modulus < 1 MPa - Stretchability > 400% - Toughness 3300 J m^{-2} - Mech./elect. stability (10000 cycles) - 3D printing	40
PAA-templated PEDOT:PSS	2.5×10^{2}	- Modulus ~ 25 kPa - Stretchability ~ 610% - Toughness 1 MJ m^{-3}	37
ohPEI/PAA hydrogel	2.6×10^{-3}	- Extensibility ~ 12298% - Adhesive strength 29.6 MPa	36
Pani/CNC/PAAm hydrogel	2.2×10^{-1}	- Modulus ~ 30 kPa - Stretchability ~ 2400%	38
PAAm/PANi-decorated PEDOT:PSS/	2.4×10^{1}	- Modulus ~ 14.1 kPa - Stretchability ~ 358% - Toughness	39

		297.7 J m^{-2}	
Conductive fillers-incorporated hydrogel			
LM/CNT embeded PAAm hydrogel	9×10^{-1}	- Stretchability ~ 2200% - Transparency ~ 93% - Self-healing	30
Ag flakes embeded PAAm-alginate hydrogel	3.7×10^{2}	- Modulus < 10 kPa - Stretchability ~ 250%	33
Ag flakes/LM embedded PVA-Borax gel	7.0×10^{2}	- Modulus ~ 20 kPa - Stretchability > 400% - Self-healing - Anti-drying	34
PVA/P(AAm-co-SMA)/LM and Ni NWs	1.1×10^{2}	- Modulus ~ 89 kPa - Stretchability ~ 481% - toughness ~ 721 kJ m^{-3}	31
Gold nanosheets embedded into an AA, PVA and AA- NHS hydrogel via sequential formation	5.6×10^{2}	- Modulus ~ 388 kPa - Stretchability ~ 240% - Charge injection capacity ~ 8.3 mC cm^{-2}	32
ANF-PVA/Ag NWs hydrogel	1.7×10^{2}	- Tensile strength ~ 5.5	35

		MPa - Modulus ~ 15.4 MPa	
Conductive materials-coated hydrogel			
LM-printed P(AAm-co-MAAc)	2×10^3	- Stretchability ~ 630% - Self-shaping	42
Carbon electrode-coated Nafion	7.8×10^2	- Modulus ~ 1330 MPa - Stretchability ~ 20% - Electrochemical activity	43
Pt-reduced Nafion	4.0×10^3	- Modulus ~ 150 MPa - Electrochemical activity	44
Au cluster-assembled PAA-co-PAN hydrogel	1.0×10^3	- Modulus ~ 0.35 MPa - Stretchability ~ 255% - Electrochemical activity	45
Au NPs assembly on PAA-based hydrogels	4.3×10^3	- Modulus ~ 4 MPa - Stretchability ~ 20% - Electroosmosis	55
PAA-co-PAAm	**8.4×10^4**	**-**	**Our**

hydrogel with TOA-Au NPs	**Modulus ~ 30 kPa - Stretchability ~ 200%**	**wor k**

*PAAm: polyacrylamide, PEDOT:PSS: poly(3,4 ethylenedioxythiophene):poly(styrene sulfonate), PU: polyurethane, PAA: poly(acrylic acid), LM: liquid metal, CNT: carbon nanotube, PVA-Borax: polyvinyl alcohol-borax, P(AAm-co-MAAc): poly(acrylamide-co-methacrylic acid), PAA-co-PAN: poly(acrylic acid-co-acrylonitrile), AA: acrylic acid, PVA: polyvinyl alcohol, AA-NHS: acrylic acid N-hydroxysuccinimide ester, ohPEI: oxidized polyethyleneimine, Pani: polyaniline, CNC: cellulose nanocrystal, ANF: aramid nanofiber, Ag NWs: silver nanowires, TOA-Au NPs: tetraoctylammonium gold nanoparticles

Table S2. Comparison of power output and operational stability of flexible EBFCs.

Material	**Electrical Conductivity (S cm^{-1})**	**Maximum Power density (mW cm^{-2})**	**Power stability (Time span)**
TPU	-	0.06	73 % (21 days)
Tre@ZIF-8	-	0.55	65 % (5 days)
PVA/SSA-DA hydrogel	-	0.23	70 % (7 days)
Polyurethane sheet	-	0.13	-
PDMS	-	0.01	-
PAA-co-PAAm hydrogel	**1.5×10^5**	**3.70**	**80 % (30 days)**

*TPU: thermoplastic polyurethane, Tre@ZIF-8: trehalase encapsulated within ZIF-8 via biomimetic mineralization, PVA/SSA-DA: polyvinyl alcohol/succinic anhydride-dopamine, PDMS: polydimethylsiloxane.

Movie S1. Real-time interfacial visualization of capillary-driven Au NP assembly, shown from ~5 min after deposition to capture the quasi-stable morphological evolution.

References

[S1] J. Ko, C. Kim, D. Kim, Y. Song, S. Lee, B. Yeom, J. Huh, S. Han, D. Kang, J.-S. Koh, *Sci. Robot.* **2022**, 7, eabo6463.

[S2] M. Brust, M. Walker, D. Bethell, D. J. Schiffrin, R. Whyman, *J. Chem. Soc., Chem. commun.* **1994**, 801.

[S3] J. Turkevich, P. C. Stevenson, J. Hillier, *Discuss. Faraday Soc.* **1951**, 11, 55.

[S4] M. Wuithschick, A. Birnbaum, S. Witte, M. Sztucki, U. Vainio, N. Pinna, K. Rademann, F. Emmerling, R. Kraehnert, J. Polte, *ACS Nano* **2015**, 9, 7052.

[S5] E. Laviron, *J. Electroanal. Chem.* **1979**, 101, 19.

[S6] K. Zhou, Y. Zhu, X. Yang, C. Li, *Electroanalysis* **2010**, 22, 259.

[S7] M. Portaccio, B. Della Ventura, D. Mita, N. Manolova, O. Stoilova, I. Rashkov, M. Lepore, *J. Sol-Gel Sci. Technol.* **2011**, 57, 204.

[S8] A. Barth, *Biochim. Biophys. Acta - Bioenerg.* **2007**, 1767, 1073.

[S9] S. Guan, J. Wang, Y. Yang, X. Zhu, J. Zhou, D. Ye, R. Chen, H. Dai, Q. Liao, *Adv. Funct. Mater.* **2023**, 33, 2303134.

[S10] Y. Wang, Z. Kang, H. Song, Y. Wang, Z. Zhu, *Chem. Eng. J.* **2025**, 520, 165912.

[S11] Y. Yuan, Z. Zhang, J. Cao, X. Zhao, L. Ye, G. Wang, *Biosens. Bioelectron.* **2024**, 247, 115930.

[S12] A. J. Bandodkar, I. Jeerapan, J.-M. You, R. Nuñez-Flores, J. Wang, *Nano Letters* **2016**, 16, 721.

[S13] J. Lee, K. Y. Kim, Y. Kwon, D. Y. Khang, *Adv. Funct. Mater.* **2024**, 34, 2309386.